Turbulence Structure of Arctic Stratus Clouds Derived from Measurements and Calculations

JÖRG E. FINGER AND PETER WENDLING

German Aerospace Research Establishment (DLR), Institute of Atmospheric Physics, Oberpfaffenhofen, Federal Republic of Germany

ABSTRACT

Results are presented from a detailed case study of an Arctic stratus cloud over the Fram Strait that is based on aircraft measurements and model calculations. The measurements have been performed during MIZEX 1984 (Marginal Ice Zone Experiment) and include high frequency data of meteorological parameters and low frequency measurements of radiation fluxes and cloud microphysical data. The vertical mean structure of the Arctic cloud-topped-planetary boundary layer and the turbulence structure are analyzed and discussed. The main processes that contribute to the turbulent kinetic energy are identified by comparison of the measurements with the results of a one dimensional turbulence model with second-order closure. The radiative cooling at cloud top is identified to be the dominant process controlling the whole turbulence structure for the case of a quasi steady state boundary layer. In this fully developed regime the energy consuming entrainment is sustained by the shear-produced horizontal velocity variance via pressure velocity correlation.

1. Introduction

A large amount of the surface of the earth is covered by low-level stratus clouds consisting of liquid water. They modulate the planetary boundary layer (PBL) and their occurrence is often connected with areas of cold ocean water. Extended fields of stratocumulus tend to be located off the west coasts of the continents as well as over the central Arctic basin. In summer the frequency of these Arctic stratus clouds (ASC) reaches up to 85%, with a fractional coverage of 75%. On the other hand, during winter the frequency reduces to 25% with a fractional cloud cover of 15% (Huschke 1969). A rapid change in cloudiness occurs in April/May as well as in September/October. These clouds typically show large horizontal homogeneity and high persistence. The mean horizontal extent is reported by Dolgin (1960) as 460 km for stratus, in extreme cases 2000 km were reached. Cloud thickness is generally between 150 and 500 m (Dergach et al. 1966). Typical liquid water contents have been measured between 0.1 and 0.4 g m^{-3} (Tsay and Jayaweera 1984). One special case of ASC is shown in Fig. 1, observed during the Marginal Ice Zone Experiment 1984 (MIZEX 84) between Greenland and Svalbard. The cloud layer can be well identified by its homogeneous grey color, which differs strongly from the dark color of the open sea and the ice covered land. This cloud layer extends from 74° to 82°N latitude. Due to its large extent and per-

sistence, especially summer cloudiness within the Arctic basin has a significant effect on the surface radiation budget and therefore on snow and ice conditions (Shine and Crane 1984).

If we want to understand the processes forming Arctic stratus clouds, we have to understand the different mechanisms interacting in the planetary boundary layer. What are these mechanisms controlling the CTBL and how do they interact? Diabatic warming by absorption of shortwave radiation is distributed over a deep layer in the cloud and reduces the liquid water content. On the other hand, longwave cooling that takes place mostly near cloud top acts in the opposite sense. Thus, the vertical distribution of the heating/cooling rates within the cloud is far from homogeneous and may give rise to localized sources of turbulence kinetic energy. Turbulence in the PBL may also be generated by wind shear and by cooling through evaporation of cloud parcels that are entrained from the free atmosphere. This process brings warmer and drier air down into the PBL, consumes turbulence kinetic energy and may even lead to the break up of a continuous cloud deck. Whether a cloud deck will dissipate or not is also determined by the mean vertical velocity. In order to maintain a certain cloud layer against subsidence a supply of moisture from the surface is required to compensate for the amount of warm, dry air that is entrained at cloud top. The evolution of a CTBL is the result of the complex interaction of the above mentioned processes that are relevant for all types of CTBL, e.g. stable, neutral or convective ones.

In particular, Arctic stratus clouds generally differ from marine stratocumulus clouds at lower latitudes

Corresponding author address: Dr. Peter Wendling, DLR, Institute of Atmospheric Physics, D-8031 Oberpfaffenhofen, Federal Republic of Germany.
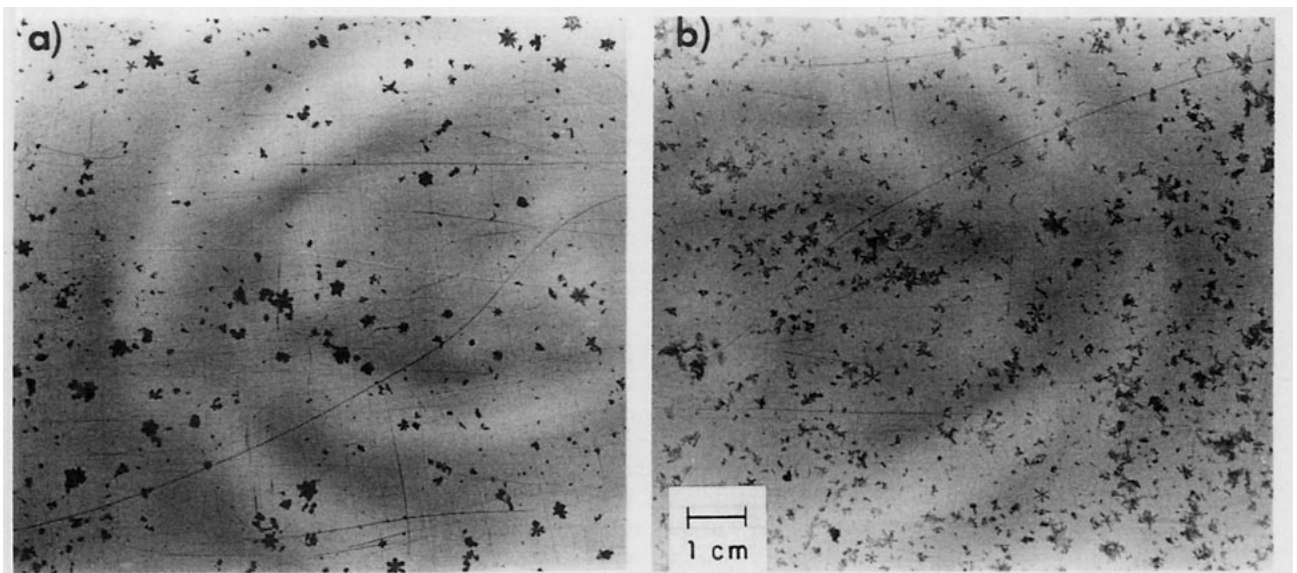
FIG. 1. Satellite picture of one case of Arctic stratus clouds at 1018 UTC 26 June 1984 that shows the difference of the equivalent radiational temperatures of NOAA-6 AVHRR channel 3 (3.55–3.93 μm) and channel 4 (10.5–11.5 μm). The area of stratus is indicated by the nearly homogeneous grey color between Svalbard (right side) and Greenland (left side). By this method, the influence of thermal radiation is reduced and the reflection of solar radiation is emphasized, allowing the low level clouds and surface of the earth easily to be distinguished, although they have nearly the same temperatures. The bright regions south and south east of Svalbard are associated with high level clouds connected to a frontal zone.

by the lower surface and cloud top fluxes and also lower liquid water content. Furthermore, solar radiation acts for the case of ASC both day and night in summer and the melting ice keeps the surface temperature constant, thus suppressing convection.

Until now, observations of ASC describing mean conditions and detailed turbulence structure have been limited to the Canadian and American regions of the Arctic. Most of the previous studies have focused on the radiative properties of the clouds in the infrared and solar part of the spectrum (Herman 1977; Herman 1980) as well as on their dependence on the microphysical cloud composition (Herman and Curry 1984; Curry and Herman 1985). Many of the cases show near cloud base an adiabatic increase of liquid water content with increasing height in clouds while the drop concentration remains nearly constant (Tsay and Jayaweera 1984; Curry 1986). The cloud morphology and internal structure depends strongly on the type of air flow in which they form as was shown by Tsay and Jayaweera (1984). According to their work, ASC tend to appear sometimes as multilayered clouds. The upper layer clouds that are not connected to the PBL are formed by advection of moist air at those levels. For the first time Curry (1986) presented a combined analysis of vertical velocity, temperature and humidity fluctuations, radiative fluxes and cloud microphysical

properties. The analysis clearly identifies the cloud top as the thermally most active part of ASC with negative buoyancy fluxes in all cases. These results were completed by the detailed description of the mean and turbulence conditions for two cases of Arctic summertime cloudiness as measured from instrumented aircraft (Curry et al. 1988).

Modeling of ASC has proceeded during the last years essentially in two main directions. The first makes use of integrating mixed-layer models that are able to simulate conditions in the CTBL at low computational expense. Budget equations of the vertically conservative variables, such as dry and moist static energy, are solved for three layers: the surface layer, the well-mixed cloud/subcloud layer, and the inversion layer (Lilly 1968; Kraus and Schaller 1978a). In order to close the system the turbulent fluxes must be specified at the mixed layer boundaries. This is rather difficult to accomplish at the cloud top, and is usually done by parameterizing the entrainment rate. The assumption is that a certain fraction of the turbulence kinetic energy (TKE) produced by buoyancy in the mixed layer, is then consumed by negative buoyancy at the top of the well-mixed layer. The role of wind shear in determining the production and consumption rates of TKE has been touched briefly by Randall (1984) but was until now not considered in integrating mixed layer models.

However, in spite of this restriction, the evolution of layered clouds can be studied for different climate regions (Kraus and Schaller 1978a; Schubert et al. 1979) under the influence of various external conditions such as large scale subsidence and advection, surface conditions, radiative fluxes above cloud top and stability of the air aloft. Applying a model of this kind of Arctic conditions at 80°N Busch et al. (1982) obtained small negative fluxes near the surface which increase to a maximum value just below the inversion and then rapidly drop to zero. No region with negative entrainment fluxes of heat is simulated, in contrast to the observations.

A second group of models consists of one-dimensional ensemble-averaged models. In these models the combined effect of all scales of turbulence on the mean variables is parameterized with methods of different degrees of complexity. Herman and Goody (1976) adopted constant exchange coefficients with height, and they first showed by their simple dynamic model the importance of radiation for the formation and dissipation of Arctic stratus clouds. In particular, they related the occurrence of two layered ASC to the absorption of solar radiation within the cloud layer. Otha (1982) and Forkel and Wendling (1986) showed that the separation of the clouds into two layers cannot be explained by absorption of solar radiation due to pure water droplets alone. Both studies are based on one-dimensional models of the CTBL that use stability dependent eddy diffusion coefficients.

One-dimensional ensemble-averaged models that apply higher order turbulence closure schemes are more detailed in their formulation of turbulence. This method solves in addition to the equations for the mean velocity, humidity and temperature, the equations for the second-order moments. Models of this type give detailed insight into the effects of several physical processes in determining the turbulent structure of the PBL and have up to now been applied either to cases of the convective boundary layer (Mellor and Yamada 1974; Andre et al. 1976; Chen and Cotton 1983b; Finger and Schmidt 1986) as well as to the CTBL (Oliver et al. 1978; Moeng and Arakawa 1980; Moeng and Randall 1984; Chen and Cotton 1983a, 1987; Chen 1985; Bougeault 1985; Duynkerke and Driedonks 1987). The models differ mainly with regard to the particular closure scheme that is applied. The accuracy of this model type in describing the vertical turbulence structure has been demonstrated by comparing numerical simulations with laboratory and field experiments (Finger and Schmidt 1986; Chen and Cotton 1987; Duynkerke and Driedonks 1987).

Despite the fact that important progress has been achieved, there remain many open questions related to the structure, formation and evolution of ASC. Measurements of the meteorological parameters relevant to the turbulence structure of ASC are restricted until now to the observations of Curry (1986) and

Curry et al. (1988). There analysis gives a plausible picture of the internal dynamics of the Arctic CTBL. However, they point out that existing cloud models, especially of the vertically integrating mixed layer type, may obscure important processes that significantly affect the CTBL energetics. As a consequence, a detailed comparison between measurements and calculations based on models considering the most relevant physical processes with respect to the turbulence structure of the Arctic CTBL is still missing. Therefore, during MIZEX 84 high frequency measurements of wind, temperature and humidity, radiative fluxes and cloud microphysical properties were carried out with the German Falcon research aircraft. The experiment took place during June and July of 1984 in the Fram Strait between Svalbard and Greenland. This paper describes the measurements, which give detailed information on the cloud morphology, the vertical profile of the turbulence fluxes and of the turbulence kinetic energy. Further, a one-dimensional statistical model with second-order closure was developed to study in detail the influence of the most important physical processes on the turbulence structure of the PBL. The model predictions of the first and second-order moments are compared with the observations. Due to the well-developed horizontal homogeneity of ASC, the ensemble-averaged model is shown to be capable of simulating the cloud structure and development. By determining components of the budget equations for the vertical velocity variance, the turbulence kinetic energy and the turbulent heat flux, the turbulent structure of the Arctic CTBL is investigated and the interaction of radiation, wind shear and buoyancy is described. The effects of radiation and large scale subsidence are demonstrated in parameter studies.

2. Description of the one-dimensional model

The structure of the cloudy boundary layer depends on radiational, cloud-microphysical and dynamical effects. For simulations of the CTBL parameterizations are needed for each of these physical processes, and must be coupled within an interactive model.

a. Dynamical part

Starting from the well-known Boussinesq system, we assume horizontal homogeneity, thus reducing the problem to one dimension in the vertical. Neglecting molecular diffusion, precipitation and ice within the cloud, the equations for the ensemble mean quantities are:

$$\frac{\partial \bar{u}}{\partial t} = f(\bar{v} - v_g) - \frac{\partial \overline{u'w'}}{\partial z} - \bar{w}\frac{\partial \bar{u}}{\partial z} \qquad (1)$$

$$\frac{\partial \bar{v}}{\partial t} = -f(\bar{u} - u_g) - \frac{\partial \overline{v'w'}}{\partial z} - \bar{w}\frac{\partial \bar{v}}{\partial z} \qquad (2)$$

$$\frac{\partial \bar{r}_t}{\partial t} = -\frac{\partial \overline{w'r_t'}}{\partial z} - \bar{w}\frac{\partial \bar{r}_t}{\partial z} \tag{3}$$

$$\frac{\partial \bar{\theta}_l}{\partial t} = -\frac{\partial \overline{w'\theta_l'}}{\partial z} - \bar{w}\frac{\partial \bar{\theta}_l}{\partial z} - \frac{1}{\rho c_p}\frac{\partial R}{\partial z}. \tag{4}$$

The prognostic mean variables are the horizontal wind components $\bar{u}$ and $\bar{v}$ in the x and y directions, respectively, the liquid water potential temperature $\bar{\theta}_l = \bar{\theta}(1 - L_v/(c_p\bar{T})\bar{r}_l)$, and the total mixing ratio, $\bar{r}_t = \bar{r} + \bar{r}_l$. Betts (1973) and Deardorff (1976) showed that $\bar{\theta}_l$ and $\bar{r}_t$ are quasi-conservative quantities for phase changes if the liquid water remains within the volume. This simplification is supported by the fact that our measurements show only a small concentration of droplets with diameters larger than 60 μm implying that collection and coalescence processes due to falling

droplets may be relatively unimportant in our case of ASC. The influence of the large scale pressure gradient is represented by the components of the geostrophic wind, u_g and v_g. The vertical velocity $\bar{w}$ depends only on height, so no prognostic equation is solved.

The unknown terms in this system are the second-order moments, i.e. the turbulent vertical fluxes of the mean quantities. Deriving the time dependent equations for these unknowns we encounter terms such as advection, production by gradient generation and buoyancy, that may be calculated directly, as well as other terms which must be parameterized, such as diffusion, dissipation and pressure velocity correlations. Using the Kolmogoroff hypothesis for dissipation and the formulations of Rotta (1951), Launder et al. (1975) and Zeman and Lumley (1976) for the pressure–velocity correlations, these equations read for single components:

$$\frac{\partial \overline{u'^2}}{\partial t} = -\bar{w}\frac{\partial \overline{u'^2}}{\partial z} - 2(1 - c_{Gm})\overline{u'w'}\frac{\partial \bar{u}}{\partial z} - \frac{\partial \overline{w'u'^2}}{\partial z} - c_{Rm}\frac{q}{l}\left(\overline{u'^2} - \frac{1}{3}q^2\right)$$
$$+ \left(\frac{2}{3}c_{Bm}\right)g(\beta_1\overline{w'\theta_l'} + \beta_2\overline{w'r_t'} + \beta_3\overline{w'r_l'}) - \frac{2}{3}c_{\epsilon m}\frac{q}{l}q^2 \tag{5}$$

$$\frac{\partial \overline{v'^2}}{\partial t} = -\bar{w}\frac{\partial \overline{v'^2}}{\partial z} - 2(1 - c_{Gm})\overline{v'w'}\frac{\partial \bar{v}}{\partial z} - \frac{\partial \overline{w'v'^2}}{\partial z} - c_{Rm}\frac{q}{l}\left(\overline{v'^2} - \frac{1}{3}q^2\right)$$
$$+ \left(\frac{2}{3}c_{Bm}\right)g(\beta_1\overline{w'\theta_l'} + \beta_2\overline{w'r_t'} + \beta_3\overline{w'r_l'}) - \frac{2}{3}c_{\epsilon m}\frac{q}{l}q^2 \tag{6}$$

$$\frac{\partial \overline{w'^2}}{\partial t} = -\bar{w}\frac{\partial \overline{w'^2}}{\partial z} - 2(1 - c_{Gm})\overline{w'^2}\frac{\partial \bar{w}}{\partial z} - \frac{\partial \overline{w'^3}}{\partial z} - c_{Rm}\frac{q}{l}\left(\overline{w'^2} - \frac{1}{3}q^2\right)$$
$$+ \left(2 - \frac{4}{3}c_{Bm}\right)g(\beta_1\overline{w'\theta_l'} + \beta_2\overline{w'r_t'} + \beta_3\overline{w'r_l'}) - \frac{2}{3}c_{\epsilon m}\frac{q}{l}q^2 \tag{7}$$

$$\frac{\partial \overline{\theta_l'^2}}{\partial t} = -\bar{w}\frac{\partial \overline{\theta_l'^2}}{\partial z} - 2\overline{w'\theta_l'}\frac{\partial \bar{\theta}_l}{\partial z} - \frac{\partial \overline{w'\theta_l'^2}}{\partial z} - 2c_{cl}\frac{q}{l}\overline{\theta_l'^2} \tag{8}$$

$$\frac{\partial \overline{r_t'^2}}{\partial t} = -\bar{w}\frac{\partial \overline{r_t'^2}}{\partial z} - 2\overline{w'r_t'}\frac{\partial \bar{r}_t}{\partial z} - \frac{\partial \overline{w'r_t'^2}}{\partial z} - 2c_{cl}\frac{q}{l}\overline{r_t'^2} \tag{9}$$

$$\frac{\partial \overline{\theta_l'r_t'}}{\partial t} = -\bar{w}\frac{\partial \overline{\theta_l'r_t'}}{\partial z} - \overline{w'r_t'}\frac{\partial \bar{\theta}_l}{\partial z} - \overline{w'\theta_l'}\frac{\partial \bar{r}_t}{\partial z} - \frac{\partial \overline{w'\theta_l'r_t'}}{\partial z} - 2c_{cl}\frac{q}{l}\overline{\theta_l'r_t'}. \tag{10}$$

Vertical turbulent fluxes.

$$\frac{\partial \overline{u'w'}}{\partial t} = -\bar{w}\frac{\partial \overline{u'w'}}{\partial z} - (1 - c_{Gm})\left(\overline{u'w'}\frac{\partial \bar{w}}{\partial z} + \overline{w'^2}\frac{\partial \bar{u}}{\partial z}\right) - \frac{\partial \overline{w'^2u'}}{\partial z} + (1 - c_{Bm})g(\beta_1\overline{u'\theta_l'} + \beta_2\overline{u'r_t'}) - c_{Rm}\frac{q}{l}\overline{u'w'} \tag{11}$$

$$\frac{\partial \overline{v'w'}}{\partial t} = -\bar{w}\frac{\partial \overline{v'w'}}{\partial z} - (1 - c_{Gm})\left(\overline{v'w'}\frac{\partial \bar{w}}{\partial z} + \overline{w'^2}\frac{\partial \bar{v}}{\partial z}\right) - \frac{\partial \overline{w'^2v'}}{\partial z} + (1 - c_{Bm})g(\beta_1\overline{v'\theta_l'} + \beta_2\overline{v'r_t'}) - c_{Rm}\frac{q}{l}\overline{v'w'} \tag{12}$$

$$\frac{\partial \overline{w'\theta_l'}}{\partial t} = -\bar{w}\frac{\partial \overline{w'\theta_l'}}{\partial z} - (1 - c_{GT})\left(\overline{w'\theta_l'}\frac{\partial \bar{w}}{\partial z} + \overline{w'^2}\frac{\partial \bar{\theta}_l}{\partial z}\right) - \frac{\partial \overline{w'^2\theta_l'}}{\partial z} + (1 - c_{BT})g(\beta_1\overline{\theta_l'^2} + \beta_2\overline{\theta_l'r_t'}) - c_{RT}\frac{q}{l}\overline{w'\theta_l'} \tag{13}$$

$$\frac{\partial \overline{w'r_t'}}{\partial t} = -\bar{w}\frac{\partial \overline{w'r_t'}}{\partial z} - (1 - c_{GT})\left(\overline{w'r_t'}\frac{\partial \bar{w}}{\partial z} + \overline{w'^2}\frac{\partial \bar{r}_t}{\partial z}\right) - \frac{\partial \overline{w'^2r_t'}}{\partial z} + (1 - c_{BT})g(\beta_1\overline{\theta_l'r_t'} + \beta_2\overline{r_t'^2}) - c_{RT}\frac{q}{l}\overline{w'r_t'}. \tag{14}$$

A down-gradient approach is made for parameterizing the triple correlations:

$$\overline{w'u_i'^2} = -c_{3m}ql\frac{\partial \overline{u_i'^2}}{\partial z} \qquad (15)$$

$$\overline{w'^2u_i'} = -c_{3m}ql\frac{\partial \overline{w'u_i'}}{\partial z} \qquad (16)$$

$$\overline{w'^2a'} = -c_{3T}ql\frac{\partial \overline{w'a'}}{\partial z} \qquad (17)$$

$$\overline{w'a'b'} = -c_{3T}ql\frac{\partial \overline{w'a'b'}}{\partial z}. \qquad (18)$$

Here, a and b represent any scalar variable. The buoyancy coefficients, β_1, β_2 and β_3 consider the influences of density fluctuations forced by temperature fluctuations, water vapor fluctuations and condensation effects. In the velocity variance equations the influence of condensation is accounted for by the correlation between fluctuation of vertical wind speed and liquid water content $\overline{w'r_l'}$, parameterized using the approach of Deardorff (1976). The terms associated with the fluctuations of the radiative heating rate are neglected in our second order equations. This simplification may be supported by the horizontal homogeneity of the observed cloud layer, although, in the case of broken cloudiness these terms may be large (Moeng 1986). The constants used in the equation system above are taken from the literature, and the same values are used by Finger and Schmidt (1986) for simulating a convective boundary layer in a water tank: $c_{\epsilon m} = 1/16.67$, $c_{\epsilon T} = 0.1$, $c_{Bm} = 3/10$, $c_{BT} = 1/3$, $c_{Rm} = 0.36$, $c_{RT} = 0.46$, $c_{Gm} = 0.0$, $c_{GT} = 0.0$, $c_{BH} = 1/5$, $c_{3m} = 1.5$, $c_{3T} = 1.1$. The zero values of c_{Gm} and c_{GT} were found to be sufficient, as numerical tests have shown. The differences between our constants and those of other authors are related to our use of q instead of $\sqrt{E}$ in the Eqs. (1) to (20).

The set of equations is closed by the length scale l. As the results are sensitive to the value of l a few more details are given on its parameterization. The formulation of Bougeault (1985) is adopted, which takes the vertical distribution of E and the thermal stability of the CTBL into account. This formulation considers the free path of an air parcel moving upward or downward against the thermal stability and thereby converting its own turbulent kinetic energy into potential energy. The conversion rate between kinetic and potential energy is assumed to be unity. Then l is a geometric average of the free path upwards l_u and downwards l_d: $l = \frac{1}{2}l_u l_d/(l_u + l_d)$.

Horizontal turbulent fluxes. Three assumptions are made for computation of the horizontal turbulent fluxes: local equilibrium, no diffusion and no vertical advection of second-order moments. These assumptions lead to four diagnostic equations:

$$\overline{u_i'\theta_l'} = \left(-\overline{u_i'w'}\frac{\partial \overline{\theta_l}}{\partial z} - \overline{w'\theta_l'}\frac{\partial \overline{u_i}}{\partial z}\right)\frac{1}{c_{RT}}\frac{l}{q} \qquad (19)$$

$$\overline{u_i'r_l'} = \left(-\overline{u_i'w'}\frac{\partial \overline{r_l}}{\partial z} - \overline{w'r_l'}\frac{\partial \overline{u_i}}{\partial z}\right)\frac{1}{c_{RT}}\frac{l}{q}, \quad i = 1, 2. \qquad (20)$$

These variables are needed in the buoyancy terms of Eqs. (11) and (12).

The equations are discretized in the vertical by the method of finite differences using a grid spacing of $\Delta z = 5$ m from the bottom up to a height of 1000 m. In Fig. 2 the arrangement of first-, second- and third-order moments is shown. We use this kind of staggering to involve only two gridpoints when a vertical divergence of a flux is needed, e.g.:

$$-\frac{\partial \overline{w'\theta_l'}}{\partial z}\bigg|_K = -\frac{\overline{w'\theta_l'}|_K - \overline{w'\theta_l'}|_{K-1}}{z|_{K+1/2} - z|_{K-1/2}},$$

$K = $ index of gridpoints.

In this kind of staggered grid, mixed terms such as gradient production terms are sensitive to different discretizations. By numerical tests we choose the following approximation, e.g. the production of u'^2 in Eq. (5) reads:

$$-2\overline{u'w'}\frac{\partial \overline{u}}{\partial z}\bigg|_K$$

$$= -\left(\overline{u'w'}|_K\frac{\overline{u}|_{K+1} - \overline{u}|_K}{z|_{K+1} - z|_K} + \overline{u'w'}|_{K-1}\frac{\overline{u}|_K - \overline{u}|_{K-1}}{z|_K - z|_{K-1}}\right).$$
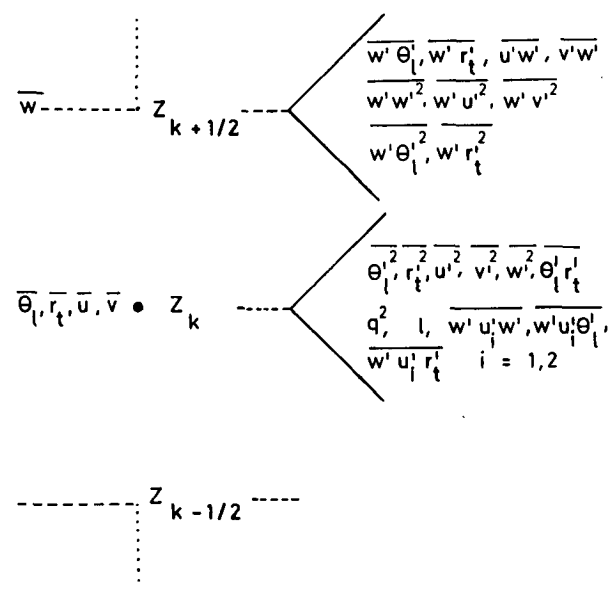

FIG. 2. Numerical grid and vertical arrangement of the variables in a staggered discretization. The height is denoted by the index k, the center of a single mesh by (●) and the boundary of a single mesh by (- - -).

Other approximations tended to produce waves with wavelengths of $2\Delta z$ that were suppressable only by an enormous reduction of the time step. For the integration in time the Adams–Bashforth method is applied using a time step $\Delta t = 0.05$ s. Besides the realizability conditions for the second-order moments (see Appendix) no additional techniques for filtering in space or time are needed to obtain stable solutions.

At the lower boundary the no-slip condition is adopted for both horizontal wind components. Here the temperature is kept constant with time using $T_s = -1.5°C$, which is the approximate temperature of a mixture of ice and salty water. The mixing ratio of water vapor is always adjusted such that the saturation point is reached at the ocean surface. Between the surface and the first mesh center above the surface, z_2, the vertical gradient of momentum is approximated by a logarithmic wind profile for the neutral case. The profiles of $\bar{\theta}_l$, and $\bar{r}_t$ are analogously calculated using the turbulent Prandtl number of 0.74. The friction velocity is calculated from the horizontal wind variances. The approximation for the neutral case is rather good, as we satisfied these conditions in our observations: $|z_2/L| \approx 2.1 \times 10^{-3} \ll 1$. The Monin-Obuchov length L is derived from the lowest flight level. At the upper boundary we use the "zero-gradient" condition for the first moments, and all moments of higher order are set to zero.

b. Condensation and radiation

The thermodynamic prognostic variables, $\bar{\theta}_l$ and $\bar{r}_t$, are approximately constant with phase changes if the liquid water remains within the volume (Betts 1973; Deardorff 1976). The temperature and the relative humidity are calculated diagnostically from these variables. We adopted the McDonald (1963) condensation scheme, whereby the point of saturation equilibrium between temperature and vapor pressure is determined by iteration, and by that the saturation mixing ratio $\bar{r}_{sat}$ is known. The mean mixing ratio of liquid water is then given by $\bar{r}_l = \bar{r}_t - \bar{r}_{sat}$. In the case of subsaturation $\bar{r}_l$ is set to zero considering the effect that liquid water staying within the volume from the time step before evaporates immediately. $\bar{r}_l$ is a dynamically passive constituent within the cloud, i.e. precipitation as well as the flux divergence of the gravitational fallout of large water drops are neglected. In cases with drizzle precipitation this neglect would produce more cloud water and hence more longwave cooling at cloud top, thus, further enhancing buoyancy production of turbulence. The simplification in our case is supported by the fact that the measurements show only a very small concentration of droplets with mean diameters larger than 60 μm, implying that collection and coalescence processes due to falling droplets may be relatively unimportant in this case of ASC.

The turbulent liquid water flux, $\overline{w'r_l'}$, and the buoyancy flux, $\overline{w'\theta_v'}$, are calculated diagnostically from the

prognostic variables, $\overline{w'\theta_l'}$ and $\overline{w'r_t'}$. Using the Clausius–Clapeyron equation, the equation of state and the Reynolds-type averaging operator, Deardorff (1976) proposed the following approximations:

$$\overline{w'r_l'} \approx \overline{w'r_t'} - \overline{w'r_{sat}'} \tag{21}$$

$$\overline{w'\theta_v'} \approx \frac{\bar{\theta}}{\bar{T}}(1 + 0.61\overline{r_{sat}} - \bar{r}_l)\overline{w'T'} + \bar{\theta}(1.61\overline{w'r_{sat}'} - \overline{w'r_t'}). \tag{22}$$

The divergence of the net radiation flux $-(\rho c_p)^{-1}(\partial R/\partial z)$ represents an important source or sink term in Eq. (4) for the liquid water potential temperature. For the calculation of the shortwave and longwave radiative fluxes and cooling rates a radiation model is employed that was developed by Zdunkowski et al. (1982) for the use in circulation and climate models. It includes the radiative effects of water vapor, CO_2, NO_2, O_3, aerosol and cloud particles with arbitrary vertical distribution and cloud fractional coverage. Multiple scattering is handled with an improved flux method in the solar spectrum and the atmospheric infrared window region. For integration, the solar spectrum has been divided into four suitable subregions. An extended emissivity method is used to treat the remaining infrared spectrum.

The required extinction and absorption coefficients and the asymmetry factor of the phase function for the water droplet size distribution functions are calculated with Mie theory. Presently four droplet size distributions can be used, which are selected as function of the liquid water content in order to cover nearly all reasonable atmospheric situations. Stratus type clouds are approximated by a size distribution according to Best (1951). Several types of aerosol size distributions are distinguished that are mainly valid for boundary layer investigations. In our case a special dataset representing clean Arctic summer conditions has been established. The influence of humidity on the extinction parameters of aerosol particles is taken into account following Hänel and Lehmann (1981).

The interactive coupling between our dynamical and the radiative part of the model is done by the transfer of profiles of temperature, relative humidity, liquid water content and cloud coverage (either 0% or 100%) to the radiative model. The profile of the atmospheric variables above 1000 m is taken as constant with time. Cooling or heating rates are calculated, and then transferred back to the dynamical model where they are used to solve the temperature equation. The vertical resolution of the radiation model is identical to that of the turbulence model in the lowest 1000 m. Above this height the grid sizes are enlarged to allow radiational transport to a height of 50 km. As the time rate of change of the concentration of atmospheric constituents is small, the time rate of change of the radiation field is also small. Therefore, incurring only a small error, the radiation subprogram is called every five

minutes of integration time, as well as every time when cloud top changes by one or more gridpoints.

3. Description of the experiment and data analysis

The Marginal Ice Zone Experiment was conducted in June and July 1984 in the area of the Greenland Sea. The main purpose was to obtain a better understanding of the influence of the ice edge on the heat and momentum fluxes in the ocean and the atmosphere (Johannessen 1987). In this region and during this season the frequency of ASC is very high. The DLR took part in this experiment performing measurements with the atmospheric Falcon 20 research aircraft. In addition, radio soundings were performed by four participating research vessels. A receiver station in Tromso, Norway recorded the data of the NOAA-6 and NOAA-7 satellites. The Falcon is equipped with sensors that are able to measure the standard meteorological parameters such as complete wind vector, temperature, humidity and pressure with a sampling rate of 100 Hz associated with a mean aircraft speed of $u_F \approx 100$ m s^{-1}. The majority of the Falcon instrumentation and its performance has been described in previous papers (Hauf 1984; Meischner 1985) and are not repeated here. However, some discussion is necessary because of the use of existing sensors within cloud. Air temperature was measured with a Rosemount total temperature probe mounted on the fuselage. Although this probe is designed to prevent water droplets from impinging on the sensor, under various conditions the sensor can become wet. Therefore, we looked for correlations between the variables r, r_l, and T which might indicate wetting. We detected no systematic variations of the correlations within clouds. Further, if the sensing wire would be wet we should notice a depression in the measured temperature after leaving the cloud due to evaporating cloud drops. However, we did not find such a depression and therefore assume that the probe was little affected by liquid water.

Specific humidity fluctuations were measured with a Lyman-α instrument mounted in a separate channel equipped with a Rosemount housing for the air inlet. Wetting of this instrument would be indicated by a slope of the humidity fluctuation power spectra steeper than $-\frac{5}{3}$. However, no change of steepness of this kind was observed at any leg within clouds and it is therefore assumed that any effect of wetting of the instrument can be ignored in the data.

Cloud droplet sizes and concentrations were recorded by Knollenberg probes FSSP and OAP-230X, as well as long- and shortwave radiative fluxes by Eppley Pyrgeo- and Pyranometers. During the experiment the FSSP was operated in the droplet diameter range of 2–32 μm and resolved into 15 equal size classes, i.e. 2 μm bins. The OAP-probe was operated in the 20–600 μm range and resolved into 30 equally spaced channels, i.e. 20 μm bins. After correction of the overlapping effects of both probes the mean liquid water content was computed by producing 1 sec averages from the concentration measurements. On the other hand, the turbulent liquid water flux was determined from data originally sampled with 10 Hz.

During the whole duration of MIZEX 84 seven experimental flights were performed for the ASC program. We will report here on the measurements of 26 June 1984 (flight number 1073). On this date we found an ideal case of ASC. Its synoptic situation and the area of our measurements (80°N, 4°E) are plotted in Fig. 3. No broken cloudiness was observed within the experimental area. The ocean was covered approximately by $\frac{4}{8}$ ice in the form of drifting floes that were rather uniformly distributed in the area. The surface temperature was about -1.5°C.

a. Synoptic situation

The distribution of surface pressure for 0000 UTC June 26 in the area of the Arctic polar basin is dominated by a cyclone (995 hPa) located above the Beaufort Sea and an anticyclone (1025 hPa) east of the Soviet island of Novaya Zemlya. Accordingly there is an advection of warm air from lower latitudes into the region of the Fram Strait. Connected with the anticyclonic curvature of the isobars is a large scale subsidence that may contribute to the formation of an inversion in the temperature profile. At the surface the advection of warm air was already established at 0000 UTC 26 June and therefore at the time of our measurements (1600 UTC) a large homogeneous field of ASC was fully developed (s.a. Fig. 1). The ASC field broke up
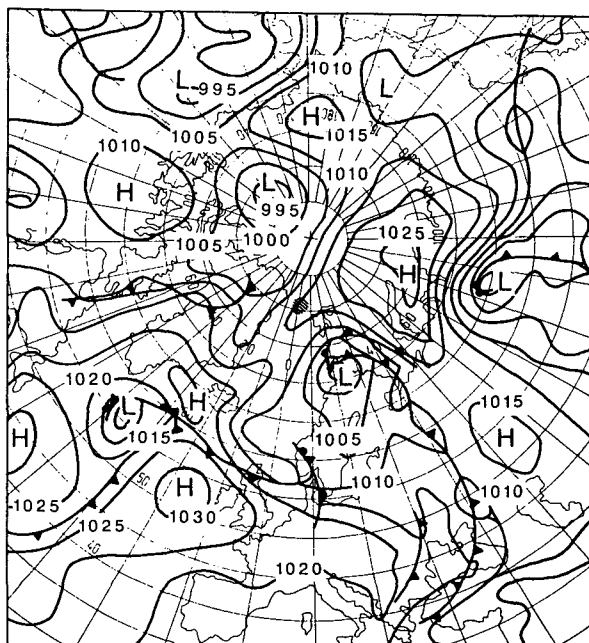
FIG. 3. Synoptic situation for 0000 UTC 27 June 1984 from the *European Meteorological Bulletin* edited by the German Weather Service. The area of the aircraft measurements is hatched.

between 1700 UTC 26 June and 0000 UTC 27 June due to the passage of a cold front which arrived from the west and produced snow showers and a wind shift to a northerly direction. The persistence of this ASC case was about two days.

b. Experimental design

When developing the flight pattern we considered two important points: first we wanted to get as much information as possible about the vertical structure of the CTBL. This required a large number of horizontal flight legs at different heights, for which each had to have a long enough time series to guarantee stable statistics. Second the Falcon has a limited endurance time of three hours for flights in the PBL. Considering the travel time from Svalbard to the experimental area, only 1.0 to 1.5 hours remained for the measurements. Bearing this in mind, we performed our measurements in seven different flight legs, which had lengths between 12 and 60 kilometers. Taking the height of the inversion $z_i \approx 400$ m as a typical scale for the boundary layer phenomena, the shortest flight leg should contain on the order of 12 km/400 m = 30 samples of such phenomena. For the other flight legs this ratio is much better.

The height of the inversion is determined from the temperature profile, that is recorded during the descent at the beginning of measurements. Because of the remarkable temperature inversion it was possible to perform one flight leg exactly at the height z_i (that corresponds to the cloud top) and to determine directly the exchange between CTBL and free atmosphere. In the case of flight 1073 we found a weak horizontal inclination of the inversion in the north–south direction. Because of this inclination and the inaccuracy of the aircraft's autopilot in flying at a defined level, the measurements were taken during the first half of the flight leg ($\sim$18 km) above and the second half ($\sim$12 km) inside the cloud top. Both parts are regarded as independent distances for averaging and are analyzed separately. The vertical resolution of our measurements is about $\Delta z = 5$ m in the region of cloud top.

c. Data analysis

In this paper we want to quantify the processes that determine the steady state ASC. Therefore, the data are analyzed to give the values of the terms of the balance equations for $\bar{\theta}_l$, $\overline{w'^2}$, E and $\overline{w'\theta'_l}$.

After correction of systematic errors such as adiabatic warming (Meischner 1985) or motion of the aircraft itself (Hauf 1984), the time series must satisfy three criteria before the data are used for further analysis: (i) the flight path must be linear, with (ii) no change in air mass, and (iii) no change in height above sea level. From such time series the mean values were calculated for each flight leg. After that the linear trends of the data were eliminated, if necessary, in order to

suppress large scale effects on turbulent moments. As the flight track was parallel to the mean wind direction in the boundary layer ($\sim$200°), the wind components u and v of the natural coordinate system are the along and cross wind components after a transformation of the coordinate system. In all further discussions we will use these transformed wind components. From the time series of physical data the variances, covariances and triple correlations were derived.

The dissipation rates of $\overline{u'^2}$, $\overline{v'^2}$ and $\overline{w'^2}$ were calculated from the inertial subranges of their individual spectra. Starting from the $-5/3$ law of the inertial subrange for atmospheric motions at high Reynolds numbers, the equation for spectral density S_u is, after the transformation from wavenumber to frequency:

$$S_u(f) = a_s \left(\frac{u_F}{2\pi}\right)^{2/3} \epsilon^{2/3} f^{-5/3} \qquad (23)$$

where f is the frequency and ϵ is the dissipation. The spectral constant is $a_s = 0.51$ for the along wind and $a_s = (4/3)0.51$ for the cross wind components, taken from Brost et al. (1982). From Eq. (23) the individual dissipation rates ϵ_u, ϵ_v and ϵ_w are derived. The dissipation rate ϵ for E is then the mean of these three values. According to the theory of isotropic turbulence ϵ_u, ϵ_v and ϵ_w should be identical, but in the case of real measurements there are differences. The standard deviation of the single measurements is not larger than 15% of their mean.

Horizontal homogeneity with reference to second- and third-order moments is tested by carrying out the averaging procedure first for the whole flight leg and then separately for the first and second half of each flight leg. If the three different means agree, the leg is considered horizontally homogeneous; otherwise the differences are a measure of the inhomogeneity. However, we are aware of the fact that the determination of more accurate third-order moments would need much longer flight legs than we could carry out (Wyngaard 1973).

4. Results of measurements and simulations

Before discussing the results of our measurements and simulations in detail, we give the characteristic values of the CTBL of this case study in Table 1. z_i is the inversion height, where $\overline{w'\theta'}$ reaches a minimum, Δh_i is the thickness of the inversion, defined by the range where $\partial\theta/\partial z > 5$ K/100 m, z_b is the height of cloud base above surface. The values of u_*, θ_* and r_* are derived in the same way as Brost et al. (1982), using the measurements from the lowest flight leg (90 m). The sign and the magnitude of θ_* and r_* indicate that this is a case of light convection and the value of the dimensionless stability parameter $|z_i/L|$ shows additionally that the turbulence structure is not dominated by the surface heat flux and that its influence is unimportant at cloud top.

TABLE 1. Characteristic values of flight 1073.

z_i (m)	Δh_i (m)	z_b (m)	u_* (m s^{-1})	$-\theta_*$ (K)	$-r_*$ (g kg^{-1})	z_i/L
410	40	170	0.35	$5.7 \cdot 10^{-3}$	$11 \cdot 10^{-3}$	-0.35

a. Initial conditions of the model

The initial values for the first moments were taken from the smoothed data of the descent at the beginning of the aircraft measurements and are plotted in Fig. 4. The large scale forcing by pressure is represented by the components of the geostrophic wind u_g and v_g which were assumed to be constant with height and time and equal to the measured wind components of the free atmosphere. This assumption is done caused by lack of large scale pressure data at different heights. The vertical velocity component was set as $\bar{w} = 0.0$ m s^{-1}. All initial profiles of second-order moments were also set to zero, except for the turbulence kinetic energy at the lowest level, set arbitrarily as: $q^2 = 0.6$ m^2 s^{-2}, which implies $u'^2 = v'^2 = w'^2 = 0.2$ m^2 s^{-2}. These are typical values for the PBL, but for the numerical solution it is unimportant, as numerical tests have shown. The surface fluxes were computed using $z_0 = 5.0 \times 10^{-3}$ m, taken from Guest and Davidson (1987).

At the beginning of the time integration, the vertical distributions of the turbulence energy and of the turbulent fluxes do not fit to the mean profiles because of the rough estimation of the initial values. As all variables, except $\bar{u}_g$, $\bar{v}_g$, $\bar{w}$ and T_s, are adjustable, the model needs some time to compute the correct turbulence structure corresponding to the prescribed physical conditions. This time is called the *adjustment time* and amounts approximately to one hour. In Fig. 5a the time and height dependent evolution of E is plotted. Initially E grows at the bottom because of surface friction. Twelve minutes later energy production starts at z_i, caused by thermal destabilization due to radiative cooling. After 18 minutes a very high amount of E is reached with an absolute maximum of about 0.9 m^2 s^{-2} at a height of $z \approx 200$ m. After passing through a relative minimum at 30 minutes, turbulence energy reaches a quasi stationary state at 60 minutes integration time. In Fig. 5b the profiles of E are shown for different time periods. Starting with the initial profile A (zero except the value at surface), profile D is asymptotically reached after passing the states of too high (profile B) and too low (profile C) turbulence energy. The profiles that are obtained after the *adjustment time* are compared with our measurements.

b. Profiles of first-order moments

Figure 6 shows the measured profiles derived from the descent and from the different horizontal flight legs, as well as the calculated profiles after the adjustment time. The profiles of mean wind speed demonstrate a

well mixed CTBL, connected with a wind jump ($\Delta u \approx 3.5$ m s^{-1}) from the wind in the boundary layer to the geostrophical wind above inversion. Below z_i a significant turbulence intensity is indicated by the high variability of the profiles. The differences between the observations themselves are caused by the different periods of averaging. While for the descent the averaging time is one second, the means of each flight leg are computed for the whole duration of the flight leg. The main features of the temperature profile, shown in Fig. 6c include the strong inversion with a jump of $\Delta\theta \approx 4.5$ K in a thin layer of $\Delta h_i \approx 40$ m and weakly stable subcloud and cloud layers.

The profile of the total mixing ratio (Fig. 7a) shows a well mixed PBL, a remarkable jump of about $\Delta r_t \approx -1.1$ g kg^{-1} at z_i, and a dry troposphere at higher altitudes. The profile of liquid water content is shown in Fig. 7b. The cloud base is located at $0.4z_i$; from this height $\hat{r}_l$ increases adiabatically up to $0.9z_i$. In the inversion zone $\hat{r}_l$ is subadiabatic, which is a typical feature for the entrainment of dry air from above and the subsequent evaporation of cloud droplets. The vertical distributions of droplet concentration and mean diameter are plotted in Fig. 7c and 7d. The constancy of concentration and the monotonic increase of mean diameter with height indicates that the growth of droplets by condensation is the dominant microphysical process in this case of stratus clouds.

c. Balance of temperature

The local time derivative of $\bar{\theta}_l$ is controlled by turbulent mixing, vertical advection and radiative cooling [see Eq. (4)]. When comparing the measured and simulated balances we have to bear in mind, that the measured balance (Fig. 8a) has a poor vertical resolution with respect to the simulations. At the left-hand side of this figure the different heights of observations are marked and the resulting values for the cooling rates are integrated values for every layer of roughly 50 m. The agreement of maximum cooling rates of about -6 K d^{-1} is very good. The observations at z/
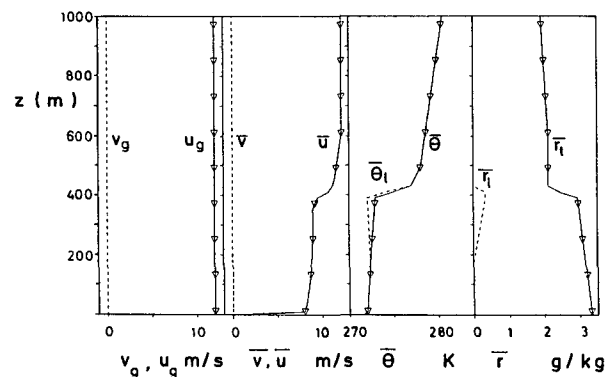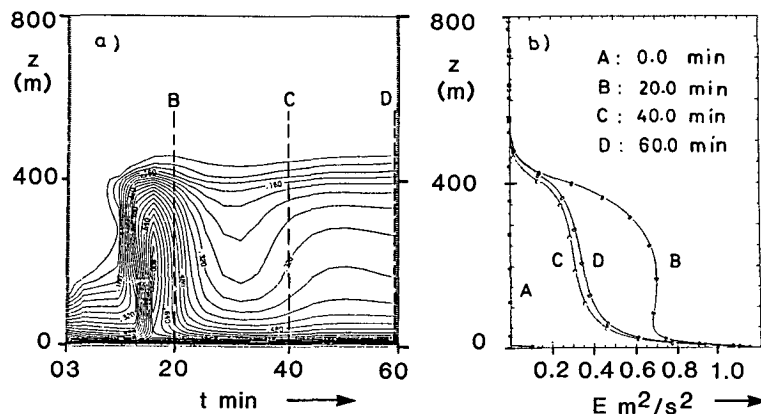

FIG. 4. Initial profiles of mean values for flight No. 1073.

FIG. 5. Evolution of turbulent kinetic energy (E) during adjustment time (t): (a) height (z) vs time development of contour lines of E (m² s⁻²), distance of contours 0.04 m² s⁻² and $E_{max} \approx 0.9$ m² s⁻²; (b) height vs E at different times denoted by lines A, B, C and D.

$z_i \approx 0.9$ show substantially lower values for the turbulent mixing term than the calculations, probably due to the poor vertical resolution of the flight legs near the inversion. The residual, R_θ, includes local time derivative, possible vertical advection, condensation and errors of the measurement. Its large value between $z/z_i = 0.8$–1.0 can be reduced by assuming a mean subsidence of the order of 10^{-2} m s⁻¹. For this value the vertical advection term $-\bar{w}(\partial\theta_l/\partial z)$ with the measured temperature jump amounts to 10^{-3} K s⁻¹. This is just the magnitude of the sum of the other balance terms. As the subsidence velocity is only known qualitatively (section 5b) this estimate is not included into Fig. 8a.

The simulated budget allows a more distinct analysis. As $\bar{w} \equiv 0.0$ m s⁻¹ is assumed, the vertical advection gives no contribution and the remaining effects have

to balance each other exactly, if a stationary situation is reached. In Fig. 8b the simulated terms of the balance Eq. (4) are plotted. The local time derivative is strongly negative just above z_i. In this region the atmosphere is cooled and cloud top rises. The physical reason for this effect is the mixing of cold air from the CTBL with the potentially warmer air of the free atmosphere. The radiative cooling is most efficient in a small region of 10 m (two grid points in the model resolution) just below z_i, and then decreases to small values in the lower 20–30 m. The radiative cooling is not completely compensated by turbulent mixing ($-\partial\overline{w'\theta'_l}/\partial z$). However, the total resulting cooling at cloud top can be offset by heating through a possible vertical advection of temperature in the range of 10^{-3} K s⁻¹ as mentioned before. Note, that Chen and Cotton (1987) too found a balance of radiative cooling, turbulent mixing and heating by large scale subsidence. In the lower part of
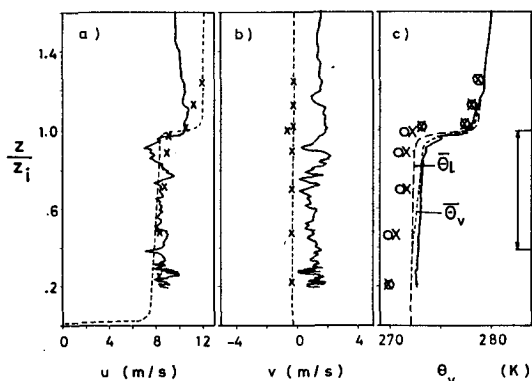

FIG. 6. Vertical profiles of wind components and temperature. The solid line represents the measurements during descent and the crosses represent measured averages of each flight leg. The dashed lines mark the simulations at one hour of simulation time. In curve c) open circles denote measured average values of θ_v on the first half of flight leg and crosses those of the second half of flight leg. The wind components u, v are given in the natural coordinate system. The double arrow indicates the vertical extent of the stratus cloud.
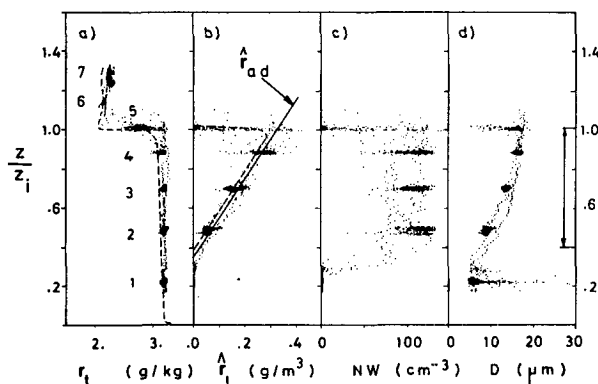

FIG. 7. Vertical profiles of total mixing ratio and liquid water content as well as of cloud microphysical variables. NW denotes the number of droplets per cubic centimeter, D the mean diameter of cloud drop size distribution. Every point is a 1 s mean value of the whole flightpattern while numbers 1 . . . 7 indicate single flight legs. The dashed line represents the model results.
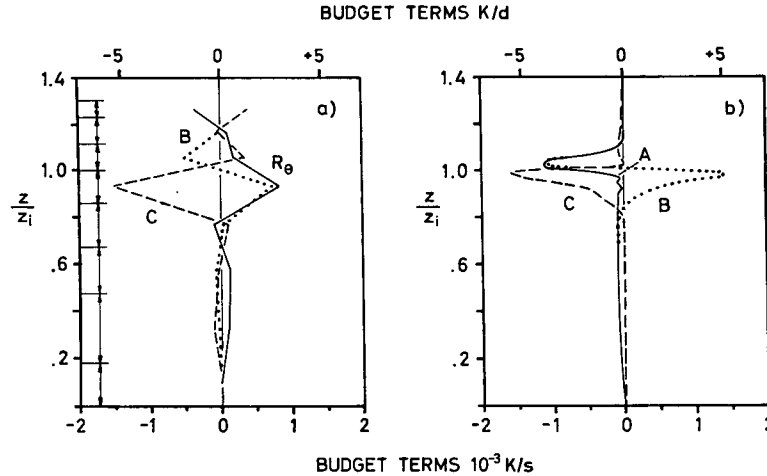
BUDGET TERMS K/d

FIG. 8. Balance of the temperature equation as function of normalized height z/z_i: (a) measurements, (b) simulations; the single terms are described by: $A = \partial\bar{\theta}_l/\partial t$, $B = -\partial\overline{w'\theta'_l}/\partial z$, $C = -(\rho c_p)^{-1}\partial R/\partial z$, $R_\theta = +\partial\overline{w'\theta'_l}/\partial z + (\rho c_p)^{-1}\partial R/\partial z$.

the cloud radiative cooling rate changes sign. But the cooling by the turbulent heat flux (curve B) dominates in this region, leading to a negative local time derivative for the whole CTBL.

Both, observed and calculated balances show that the radiative cooling is partly compensated by the vertical divergence of the turbulent heat flux. In order to answer the question what the sources of the vertical turbulent heat flux are and by which process it is controlled the whole turbulence structure of the CTBL must be investigated because all of the involved variables are coupled.

d. Profiles of velocity variances and momentum flux

To demonstrate the high degree of horizontal homogeneity, in the following figures the different means (section 3b) are plotted for each second-order moment.

The most important variable for describing the turbulence structure of any boundary layer, is the turbulence kinetic energy. In our case (Fig. 9) the profile exhibits a well-mixed CTBL with $E > 0.25$ m^2 s^{-2} below z_i and negligible E above z_i. In the surface layer ($z/z_i < 0.2$) the values of $\overline{u'^2}$, E and $\overline{u'w'}$ show maxima which are caused by the surface friction, since in that region $\bar{u}$ adjusts from 0 m s^{-1} at the surface to $\sim$8 m s^{-1} within the boundary layer (Fig. 6). In the surface layer $\overline{w'^2}$ is small and decreases with decreasing distance from the ground, as the vertical motions are hindered by the surface. In the region of about $0.5z/z_i$ the variance $\overline{u'^2}$ and E are nearly constant with height, while $\overline{w'^2}$ shows a small but significant maximum. Within the entrainment zone $\overline{w'^2}$ decreases to small values (25% of maximum), because the vertical motions are suppressed by the strong temperature inversion. Due to the large damping of vertical motions there is no secondary maximum of $\overline{w'^2}$ due to radiative cooling.

The secondary maximum of E at cloud top can be explained by the profile of $\bar{u}$: variance of $\bar{u}$ is produced by the adjustment from $\bar{u}$ to $\overline{u_g}$ in the thin layer of Δh_i. As $\overline{w'^2}$ is small in this region, found as well by Brost et al. (1982), the shear produced maximum of $\overline{u'^2}$ is reflected in the profile of E. The turbulent vertical momentum flux $\overline{u'w'}$ is negative (downwards) for the whole CTBL and exhibits maxima that have the same origins as maxima of the variances.

The comparison of measurements and simulations gives good agreement for E in the region $z/z_i < 0.7$, but distinct differences at the height z_i. Here the simulation does not reproduce the shear produced secondary maximum. The relative difference between measurements and simulation $\Delta E = (E \text{ (meas)} - E \text{ (sim)})/E \text{ (meas)}$ is about 0.57, as opposed to
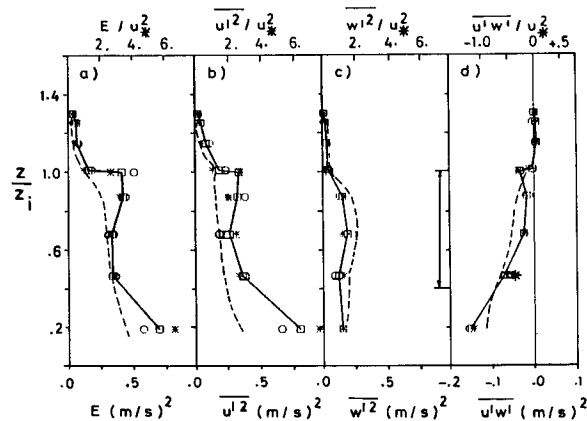

FIG. 9. Vertical profiles of velocity variances and of momentum flux. The measurements are represented by: □—average value of the complete flight leg and connected by solid line, ○—average value of first half of flight leg, *—average value of second half of flight leg. The dashed lines represent the simulations. The upper abscissa scale is normalized, the lower scale is given in SI units.

$\Delta E \approx 0.14$ at heights between 0.7 and 0.5 z/z_i. In this discussion we must account for the fact that the criteria for the horizontal homogeneity are not well fulfilled for u'^2 at inversion height, as indicated by the different means for the same height. At this point we conclude that the model is not able to simulate the profile of E in a satisfactory way at the inversion height; the reasons for this are discussed in section 4i.

e. Turbulent heat flux

The observed profile of turbulent heat flux (Fig. 10a) exhibits a typical structure. In the subcloud layer it is small and directed upwards ($\overline{w'\theta_v'} \approx 5$ W m^{-2}). This is caused by the small temperature difference between ice/water surface and the atmosphere of about $\Delta T \approx 1°C$. With this small ΔT it is impossible to get a large heat flux even if there is a high level of turbulence energy produced by shear. Inside the cloud $\rho c_p \overline{w'\theta_v'}$ increases to values of ≈ 15 W m^{-2}. Radiative cooling is most effective at cloud top. To compensate for this loss of heat, large positive heat flux is established inside the cloud. At $0.9z/z_i$ the heat flux changes sign, and at z_i becomes strongly negative ($\rho c_p \overline{w'\theta_v'} \approx -24$ W m^{-2}). At $1.01z/z_i$ that value decreases to -15 W m^{-2} and above $1.2z/z_i$ it is practically zero because of negligible turbulence kinetic energy and the slightly stable vertical gradient of potential temperature. This structure with the large entrainment flux at z_i documents the importance of the cloud top processes in driving this type of boundary layer.

We have to consider here that the entrainment consumes energy as the cold air from the CTBL is transported against the thermal stability into the free atmosphere, and vice versa. Now another question arises: What is the source of the energy needed for this transport? The convective boundary layer, which is controlled by the surface heat flux, shows an entrainment zone with $-\overline{w'\theta'}|_{z_i} \approx (0.1-0.2) \cdot \overline{w'\theta'}|_s$ as Deardorff and Willis (1985) proved by experiment and Finger and Schmidt (1986) verified by numerical simulation. However, in this case of ASC the entrainment flux $|\overline{w'\theta'}|_{z_i}$ exceeds the surface flux by about five times. This means that the surface has much less influence on the processes working at cloud top. Therefore, local effects must be responsible, such as radiative cooling and wind shear.

Regarding the vertical turbulent heat flux, the CTBL is divided into two layers, the mixed subcloud layer with small vertical heat fluxes and the cloud layer. A decoupling of these layers, such as was found by Nicholls (1984) from experiment and by Duynkerke (1987) from simulation for a case of stratocumulus over the North Sea is not found here because the high level of turbulence energy enforces a strong exchange. Brost et al. (1982) also did not find this decoupling, but they emphasized the dominance of shear-induced processes at cloud top. In their case 17-2 they argue that breaking waves might be the reason for the large

observed entrainment flux of ≈ -50 W m^{-2}. In our case there is no indication that breaking waves are involved. We analyzed the power spectra of the along wind components and did not find a significant wavelength.

Apart from cloud top the simulations show good agreement with the observations in the region between inversion and cloud base. The entrainment zone, defined by negative values of heat flux, is very well reproduced in its vertical extent as well as in its magnitude. In the surface layer the difference between observations and simulations is caused by the adopted initial and boundary conditions of the model. At the beginning of the simulation the air is warmer than the water, therefore $\overline{w'\theta_i'}$ is negative and the air is cooled. As flight legs were not possible lower than ~90 m, the aircraft measurements are unable to give results at the surface.

f. Closure assumption of mixed layer models

At this point we test the closure assumption of the mixed layer model of Kraus and Schaller (1978a). As mentioned previously, the results of this type of model are strongly dependent on the adopted closure assumption. Kraus and Schaller (1978a) argue that energy, produced by buoyancy forces, is also destroyed by negative buoyancy effects in stable stratified layers. Their formulation reads:

$$r = -\int_0^{z_i} (\overline{w'\theta_v'} < 0)dz \bigg/ \int_0^{z_i} (\overline{w'\theta_v'} > 0)dz,$$

where r is the critical value of the ratio of negative to positive buoyancy fluxes and differs for distinct climate regions. For the Arctic region Kraus and Schaller (1978b) used $r_{KS} = 0.04$. Analyzing the results of our measurements and simulations we get $r_{meas} \approx 0.14$ and $r_{sim} \approx 0.09$. Taking a 'rough' average of these values the parameter is estimated at $r_{1073} \approx 0.1$ for this case. The comparison with r_{KS} shows that Kraus and Schaller (1978a) underestimate the entrainment rate by a factor of about 2.5. Therefore, the growth of cloud top in their simulations is overestimated.

g. Humidity flux and variances of thermodynamic variables

In order to minimize in-cloud wetting of the humidity sensor the cloud layer was left upwards after two in-cloud legs to perform two flight legs in the free atmosphere. After that the final legs were flown in cloud. The profile of moisture flux derived from measurements and simulations is positive (directed upward) over the total area. In the surface layer the latent heat flux exceeds sensible by a factor of three. This is the reason for the difference between $\rho c_p \overline{w'\theta_i'}$ and $\rho c_p \overline{w'\theta_v'}$ in the subcloud layer. Evaporation at the ocean surface increases the moisture content at the lower boundary, which is then mixed by turbulence to upper
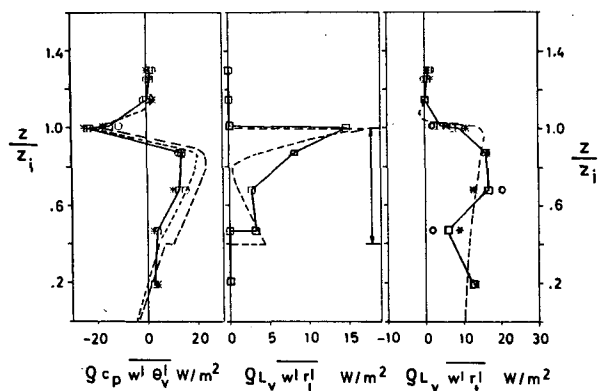
FIG. 10. Vertical profiles of fluxes of heat and moisture: symbols same as in Fig. 9. The left panel shows in addition to the variable denoted in the graph the simulated variable $\rho c_p \overline{w'\theta'_l}$ (shortly dashed).

regions. At the upper boundary of the PBL moisture is diluted by entrainment of dry environmental air. As this dilution is larger than the import from the surface, the total amount of moisture decreases in the whole boundary layer. This fact and the time dependent cooling of the whole boundary layer are the reasons why the cloud layer does not grow rapidly from its base to the ground.

Figure 10 illustrates the turbulent flux of liquid water, $\rho L_v \overline{w'r'_l}$ that has been determined by the correlation of the 10 Hz liquid water content (PMS-probe) and 10 Hz vertical velocity data. The latter have been averaged from the original 100 Hz measurements. The maximum at cloud top indicates an evaporation of droplets, caused by the downward mixing of dry air into the cloud layer. This process yields a negative fluctuation of r_l with a corresponding negative fluctuation of w. On the other hand, part of the turbulent flux of liquid water is probably caused by the warmest in-cloud parcels having the largest liquid water content. The

small vertical extent of this zone with strong positive values demonstrates that the entrainment process is limited to the upper part of the cloud layer. This is also reflected in the profile of $\bar{r}_l$, which shows subadiabatic values there (Fig. 7). In the region between $0.5z/z_i$ and $0.8z/z_i$ both $\bar{r}_l$ and $\overline{w'r'_l}$ increase with height; hence, the flux is countergradient to a high degree. At cloud base condensation dominates the profile. If a saturated air parcel is lifted by a positive w' above the condensation level, the liquid water content increases by the freshly condensed part and causes a positive r'_l. If this is the primary mechanism, the mean correlation product $\overline{w'r'_l}$ is also positive. The agreement between simulation and measurement demonstrates the usefulness of Deardorff's parameterization of the turbulent liquid water flux [Eq. (21)].

The vertical distributions of the variances $\overline{\theta'^2_l}$, $\overline{r'^2_t}$ and of the covariance $\overline{\theta'_l r'_t}$ are shown in Fig. 11. Small values are found throughout the boundary layer, except for extreme values in the entrainment zone. This behavior is predicted by the profiles of the mean values (Figs. 6 and 7), as in the mixed layer no large fluctuations are possible for the air parcels displaced in the vertical direction. On the other hand, in the entrainment zone even small vertical motions cause large fluctuations because of the strong vertical gradients there. The model estimates are generally lower than the measurements, especially for $\overline{\theta'^2_l}$ and $\overline{r'^2_t}$.

h. Triple correlations

The profiles of triple correlations, e.g. the vertical turbulent fluxes of the second-order moments q^2, $\overline{w'^2}$, $\overline{w'\theta'}$, $\overline{w'r'}$, $\overline{\theta'^2}$ and $\overline{r'^2}$, are shown in Fig. 12. In order to check the statistical significance of the measured profiles we calculated the triple correlations for the full flight leg as well as for the first and second half of each leg, just as we did for the second-order moments. Although a crude approximation for the sim-
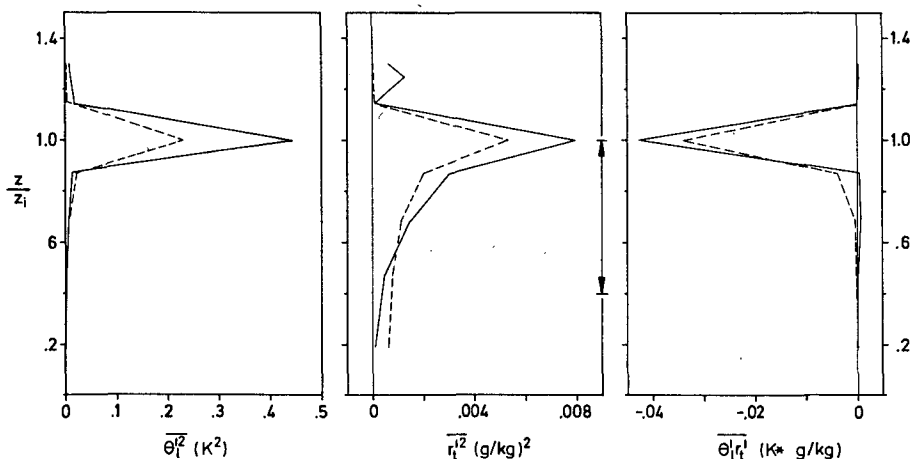

FIG. 11. Observed and calculated vertical profiles of variances of thermodynamic variables.
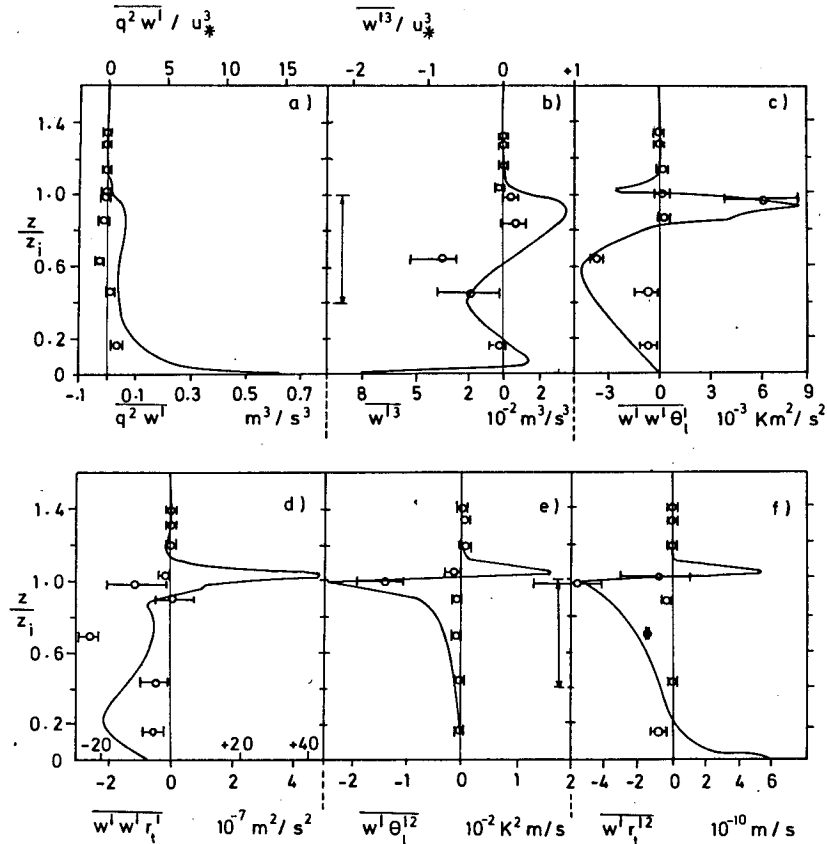Only leg averages are shown for the measured values (full line).

FIG. 12. Vertical profiles of turbulent transports of second order moments. The solid line represents the simulation and the circles (O) represent the measurements averaged over the whole flight leg. The bars indicate the range for the measured triple moments averaged over the first and second half of each flight leg. The upper scaling in (d) is valid for the observations, the lower scaling for the simulations. In addition, the variables have been normalized in (a) and (b). The double arrow marks the cloud layer. Note that the simulated correlations with θ_l and r_t are compared with measured correlations of θ and r.

ulations of third-order moments is adopted, the results show some agreement with measurements, giving at least the same order of magnitude. This refers only to the correlations $q^2 w'$ and w'^3 where the same variables are used both in simulation and measurement. For these variables the down gradient approach and the related choice of the constant c_{3m} seems to be sufficient. We are aware that the direct comparison of the remaining triple correlations in Fig. 12 is not allowed. However, we think that they are worth presenting here. At least the measured profiles show considerable statistical significance.

i. Budget of turbulence kinetic energy

If horizontal advection is neglected, the turbulence kinetic energy budget is given by

$$\frac{\partial E}{\partial t} = -\bar{w}\frac{\partial E}{\partial z} - \overline{u'w'}\frac{\partial \bar{u}}{\partial z} - \overline{v'w'}\frac{\partial \bar{v}}{\partial z} - \overline{w'^2}\frac{\partial \bar{w}}{\partial z}$$
$$- \frac{\partial \overline{w'E}}{\partial z} + g\beta_1\overline{w'\theta'_v} - \frac{\partial}{\partial z}\cdot\frac{\overline{w'p'}}{\rho} - \epsilon. \quad (24)$$

For simplicity the whole buoyancy term in this equation is replaced by $\overline{w'\theta'_v}$. The terms of local rate of change, vertical advection and transport by pressure velocity correlations cannot be determined from the aircraft observations. Therefore the following simplified equation shows a balance between a residual R_E and the remaining terms:

$$0 = -\overline{u'w'}\frac{\partial \bar{u}}{\partial z} - \overline{v'w'}\frac{\partial \bar{v}}{\partial z} - \frac{\partial \overline{w'E}}{\partial z}$$
$$+ g\beta_1\overline{w'\theta'_v} - \epsilon + R_E. \quad (25)$$

The balance Eq. (25) applied to the measurements can be compared to the sum of the velocity variances [Eqs. (5) to (7)] of the model, where the pressure strain terms sum to zero and all buoyancy production is once more approximated by $\overline{w'\theta'_v}$:

$$\frac{\partial E}{\partial t} = -\bar{w}\frac{\partial E}{\partial z} - \overline{u'w'}\frac{\partial \bar{u}}{\partial z} - \overline{v'w'}\frac{\partial \bar{v}}{\partial z}$$
$$- \overline{w'^2}\frac{\partial \bar{w}}{\partial z} - \frac{\partial \overline{w'E}}{\partial z} + g\beta_1\overline{w'\theta'_v} - \epsilon. \quad (26)$$

The shear production, which shows large positive values, turns out to be the dominant term in the turbulence energy equation (curve B, Fig. 13), near the ground and near the inversion. This is similar to the results of Brost et al. (1982). On the other hand, in the middle part of the CTBL, shear production is small. Buoyant production (curve D) is positive in the cloud interior and negative near the inversion. Energy is exported by diffusion (curve C) from the cloud region to the inversion zone. The terms discussed thus far are well represented by the simulations both in sign and magnitude. Dissipation (curve E) is nearly constant with height, except in the region near the inversion where the simulated values increase and are larger than the measured ones. The structure of the simulated curve of ϵ is related to the formulation of the length scale l. If l decreases, ϵ will increase unless q decreases as $\epsilon = c_{\epsilon m} q^3/l$ is adopted in Eqs. (5) to (7). We note that even the rather complicated formulation for l that is used in the one-dimensional model does not give the correct length scale near the inversion in this case. At this time we do not know, what the vertical profile of the dissipation rate looks like, as different observations give different results. The results of Curry et al. (1988) are not conclusive in this respect. In their case 5, the ϵ profile shows a maximum at the upper cloud top, while in their case 4 no maximum is found at cloud top.

The residual R_E contains the vertical advection of turbulence kinetic energy, the local rate of change, the pressure correlation term, and all errors from measurements. A detailed analysis of these terms results shows that the dominant part is represented by the pressure term, since the other parts are small. Using typical values of $\bar{w} = -10^{-2}$ m s^{-1} and $\partial E/\partial z = (0.3$

m^2 s^{-2})/30 m, the vertical advection term $-\bar{w}\partial E/\partial z$, reaches a value of about 10^{-4} m^2 s^{-2}, which is much smaller than the R_E-term shown in Fig. 13. In the steady state $\partial E/\partial t$ is also small, as is demonstrated by the simulation. Therefore, the remaining pressure velocity correlation term essentially controls the exchange of turbulence kinetic energy between the CTBL and the free atmosphere. Our current knowledge about this term is limited and there is a need for an independent measurement of pressure fluctuations.

j. Budget of vertical velocity variance

The budget of $\overline{w'^2}$ is given by Eq. (7). However, in the following formula the three parts of the buoyancy term have been replaced by $\overline{w'\theta'_v}$:

$$\frac{\partial \overline{w'^2}}{\partial z} = -\bar{w}\frac{\partial \overline{w'^2}}{\partial z} - 2\overline{w'^2}\frac{\partial \bar{w}}{\partial z} - \frac{\partial \overline{w'^3}}{\partial z}$$
$$- \frac{c_1}{\tau}\left(\overline{w'^2} - \frac{1}{3}q^2\right) + \left(2 - \frac{4}{3}c_{Bm}\right)g\beta_1\overline{w'\theta'_v} - \frac{2}{3}\epsilon.$$

$$(27)$$

The equation that can be evaluated from the aircraft measurements is

$$0 = +2g\beta_1\overline{w'\theta'_v} - \frac{\partial\overline{w'w'^2}}{\partial z} - \frac{2}{3}\epsilon + R_w. \quad (28)$$

The different terms that contribute to $\overline{w'^2}$ are shown in Fig. 14. The dominant process is buoyancy (curve D) with a positive contribution within the stratus layer and a negative one in the entrainment zone. Compared to the budget of E, the diffusion (curve C) is now more pronounced, with a positive contribution near the inversion and a negative one within the cloud. In this case the down-gradient approximation works well for the triple correlation w'^3. Again, the measured dissipation ϵ is nearly constant with height, while the model produces a secondary maximum near the inversion probably due to the use of an incorrect length scale.

The residual R_w is determined by the local rate of change, vertical advection, pressure correlation term and measurement errors. An estimate gives neglectable local rate of change and advection using $\bar{w} = -10^{-2}/$ m s^{-1} and $\partial w'^2/\partial z = 0.1$ m^2 s^{-2}/30 m. In the inversion zone the residual R_w, essentially representing the pressure transport, is again of importance. It balances the large contribution due to buoyancy $\overline{w'\theta'_v}$. We are now able to answer the question put forth in section 4e, i.e. where the energy originates to compensate for the loss of energy caused by entrainment against the thermal stability. It is delivered from the shear-produced horizontal velocity variances. The pressure strain term transfers parts of horizontal velocity variances to the vertical velocity variance, which itself maintains the vertical exchange between CTBL and free atmosphere. The parameterization for the pressure velocity correlations seem to work well in this case (curve B, Fig.
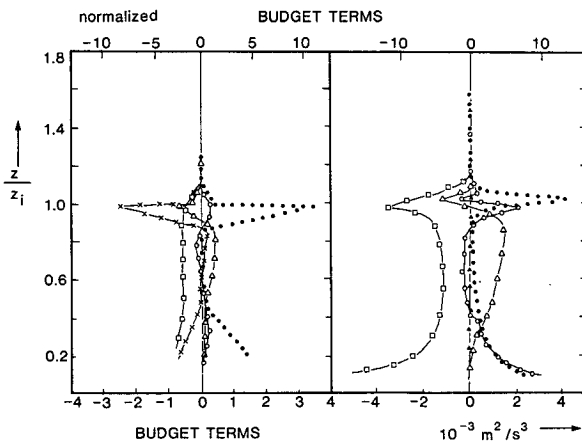

normalized   BUDGET TERMS

FIG. 13. Vertical profile of the budget of turbulence kinetic energy. The upper abscissa scale is normalized by $(\kappa z_i/u_*^3)$. The left panel represents the observations, the right panel the simulations. Single terms are described by: $B = -\overline{u'w'}(\partial\bar{u}/\partial z) - \overline{v'w'}(\partial\bar{v}/\partial z)$, $C = -\partial\overline{w'E}/\partial z$, $D = g\beta_1\overline{w'\theta'_v}$, $E = -\epsilon$, $F = \partial E/\partial t$, R_E = imbalance term (B: full circles; C: open circles; D: open triangles; E: open squares; F: full triangles; R_E: crosses).
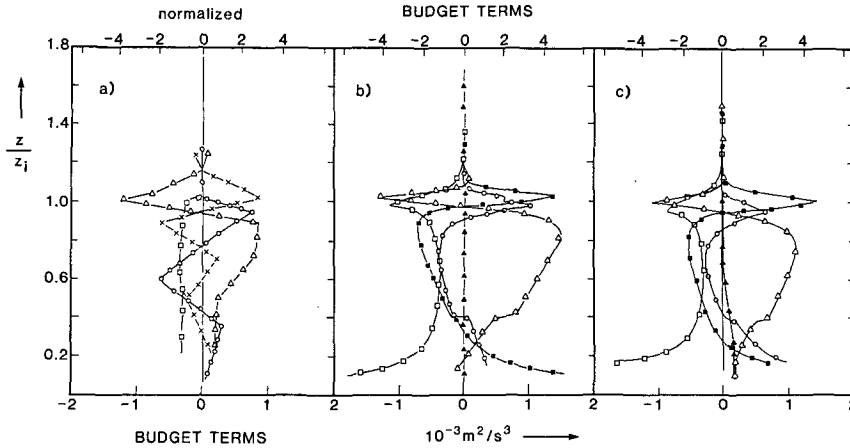
FIG. 14. Observed (a) and calculated (b, c) vertical profiles of the budget of variance of vertical velocity (curve b: vertical velocity $\bar{w} = 0$; curve c with $\bar{w}(z)$ according to section 5b). Single terms are given by: $A = -\bar{w}(\partial \overline{w'^2}/\partial z) - 2\overline{w'^2}(\partial \bar{w}/\partial z) \equiv 0$, $B = c_{Rm}(q/l)(\overline{w'^2} - \frac{1}{3}q^2) - \frac{4}{3}c_{Bm}g\beta_1\overline{w'\theta'_v}$, $C = -\partial \overline{w'w'^2}/\partial z$, $D = +2g\beta_1\overline{w'\theta'_v}$, $E = -\frac{2}{3}\epsilon$, $F = \partial \overline{w'^2}/\partial t$, R_W = imbalance term (B: full squares; C: open circles; D: open triangles; E: open squares; F: full triangles; R_w: crosses). In case c, the term A is also very small and therefore was not marked.

14). The inclusion of a realistic field of vertical velocity w (s.a. section 5b) does not significantly alter our conclusions (Fig. 14c).

k. Budget of the heat flux

Starting with Eq. (13), and neglecting the terms containing $\bar{w}$, the local rate of change of the heat flux is given by

$$\frac{\partial \overline{w'\theta'_l}}{\partial t} = -\overline{w'^2}\frac{\partial \bar{\theta}_l}{\partial z} - \frac{\partial \overline{w'^2\theta'_l}}{\partial z}$$

$$+ (2 - c_{BT})(g\beta_1\overline{\theta'^2_l} + g\beta_2\overline{\theta'_l r'_t}) - \frac{c_\theta}{\tau}\overline{w'\theta'_l}. \quad (29)$$

The equation relevant for the measurements reads:

$$0 = -\overline{w'^2}\frac{\partial \bar{\theta}_l}{\partial z} - \frac{\partial \overline{w'^2\theta'_l}}{\partial z} + 2g\beta_1\overline{\theta'^2_v} + R_{W\theta}. \quad (30)$$

Near the inversion the results of the calculations (Fig. 15, right panel) and measurements show the dominance of the gradient destruction (curve B) and the production due to buoyancy (curve D) that itself directly corresponds to the profile of $\overline{\theta'^2_l}$ near the inversion (Fig. 11). The pressure term (curve E for the simulation and curve $R_{W\theta}$ for the observations) acts as a sink in calculation and measurement. The diffusion term (curve C) transports $\overline{w'\theta'_l}$ from the boundary layer into the free atmosphere. The spikes appearing in the simulated curves are due to the fact that the time step used for the integration of the equations is close to the stability limit. The measurements underestimate the gradient destruction term (curve B) probably due to the insufficient vertical resolution. The simulated budget terms are smaller than the measured ones below $0.8z/z_i$. However, there is agreement between the structure

of both curves and it is clear that the cloud top represents the thermally most active part of the Arctic CTBL.

5. Model sensitivity studies

Thus far we considered only an instantaneous view of the structure of ASC which has been compared to the quasi steady-state solution of the model equations. In order to study the time dependent evolution of ASC we rely on a sensitivity study based on our model since no measurements have been carried out that relate to this problem. Our basic assumption for the following study is that there is no horizontal advection of first and second order moments. To initialize the field vari-
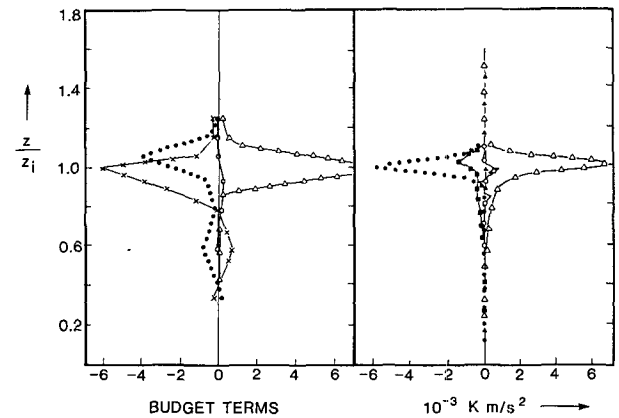

FIG. 15. Vertical profile of the budget of turbulent sensible heat flux. Single terms are given by: $A = -\bar{w}\partial \overline{w'\theta'_l}/\partial z \equiv 0$, $B = -\overline{w'^2}\partial \bar{\theta}_l/\partial z$, $C = -\partial \overline{w'^2\theta'_l}/\partial z$, $D = (g\beta_1\overline{\theta'^2_l} + g\beta_2\overline{\theta'_l r'_t})$, $E = -c_{BT}(g\beta_1\overline{\theta'^2_l} + g\beta_2\overline{\theta'_l r'_t}) - c_{RT}(q/l)\overline{w'\theta'_l}$, $F = \partial \overline{w'\theta'_l}/\partial t$, $R_{w\theta}$ = imbalance term. (B: full circles; C: open circles; D: open triangles; E: full squares; F: full triangles; $R_{w\theta}$: crosses).

ables for these parameter studies, the profiles of all prognostic variables are used, which we get after the *adjustment time*. These values are related to the time zero of the sensitivity studies.

a. The influence of radiation on the turbulence structure of ASC

Since radiative processes only indirectly impact on the state of turbulence, simulations have been performed for ASC cases with (reference case) and without radiation. For the reference case of ASC the turbulence kinetic energy E and the total liquid water content $\hat{r}_l$ are shown in Fig. 16a for two hours of development. The height of the CTBL as well as the total water content are continuously increasing. After 90 min a significant increase of E takes place starting from the surface. This is caused by the shift of the surface heat flux from negative to positive values, as the air temperature now drops below the sea surface temperature. The steady cooling of the CTBL causes cloud growth. This is partly compensated by the decrease of total mixing ratio because the turbulent export of $\bar{r}_t$ into the *free* atmosphere exceeds the import from the surface, as shown by the profile of $\overline{w'r'_t}$ in Fig. 17c.

The time dependent evolution of ASC when radiative processes are neglected is shown in Fig. 16b. First E decreases rapidly, then increases toward a new equilibrium value after 20 min. This new energy level is much lower than that in the case with radiation. In order to quantify this effect, the levels of E are listed in Table 2 and plotted in Fig. 17a. The comparison reveals a drastic decrease of E near cloud top of $\sim$90%; even at lower heights of about $0.2z/z_i$ the 23% decrease of E is still significant. As a consequence, turbulent mixing in the non radiation case becomes weak with a vanishing entrainment at cloud top, and a negative turbulent heat flux that is nearly constant with height ($\sim$4 W m^{-2} in Fig. 17b). Due to the lower boundary condition the turbulent humidity flux is positive and decreases steadily with height (Fig. 17c). The resulting small divergence leads to only weak moistening of the CTBL which is documented by a lowering of the cloud base, while at the same time cloud top height remains constant. On the whole, the cloud is thinner (280 m versus 325 m) and has a lower liquid water content (0.26 versus 0.32 g m^{-3}) than the reference case. Therefore, we conclude that radiative processes indeed have a strong influence on the cloud morphology as well as on the turbulence structure of Arctic stratus clouds. Wind shear, on the other hand is not sufficient to maintain a high level of turbulent exchange between the CTBL and the free atmosphere in this no radiation case.

b. The influence of subsidence on the turbulence structure of ASC

Before discussing the influence of large scale subsidence on ASC, we will analyze the mean vertical velocity field of 26 June 1984. The absolute accuracy of the mean vertical velocity that is determined from the aircraft measurements is about $\pm$0.5 m s^{-1}. This value is not sufficient to give the correct synoptic scale velocity of about 10^{-2} m s^{-1}. Therefore $\bar{w}$ was estimated from radiosonde soundings performed by the research vessels near our measurement area (hereafter called $\overline{w_{RS}}$) as well as from the ECMWF data analysis for 0000 UTC June 26 (hereafter called $\overline{w_E}$). For our analysis, the radio soundings of the research vessels Polarstern, Polarqueen and Hakon Mosby from 1100 UTC June 26 were used. Their positions are plotted in Fig. 18, along with the region of the aircraft measurements. For calculating $\overline{w_{RS}}$ the kinematic method proposed by O'Brien (1970) was adopted, in which $\overline{w_{RS}}$ is estimated by vertical integration of the horizontal wind divergence. For consistency $\overline{w_{RS}}$ is forced to be zero at the upper boundary. The results are plotted in Fig. 19. The data of the ECMWF analysis are available on a geographical grid with a grid size of $2.5° \times 2.5°$ at the mandatory pressure levels. The values of $\overline{w_E}$ are given in Fig. 18 for every grid point at 850 and 1000 hPa, using a minus sign for subsidence.

In Fig. 19 the results of both methods show a large scale subsidence in the lower troposphere, which was indicated by the anticyclonic curvature of the isobars in Fig. 3. But unfortunately the values of $\overline{w_{RS}} \approx -0.1$ m s^{-1} and $\overline{w_E} \approx -0.01$ m s^{-1} differ by one order of magnitude at the 850 hPa level. This difference reflects the uncertainty of these methods. For both methods the input data were very poor. While for the kinematic method only three radiosonde soundings were available, forming a highly nonsymmetrical triangle (dashed line in Fig. 18), the density of aerological data for the ECMWF-data analysis is also low in the north polar region. Although the magnitude is uncertain, in any case subsidence is prevailing in the area of the Fram Strait at the considered time.

As a consequence of warming and drying the ABL, large-scale subsidence may reduce the cloud liquid water. But besides this, are there other effects caused by subsidence? To investigate this, in the following sensitivity study a profile of non zero vertical velocity is adopted in addition to the conditions defining the reference case. The profile of $\bar{w}$ used in the simulations is indicated by the dotted line in Fig. 19. The dotted line presents a mean profile of all crosses and the shape is extrapolated by eye from the other profiles.

The time dependent evolution of the cloud structure (Fig. 16c) shows no ascent of cloud top and E is nearly the same as in the reference case. The resulting cloud is lower in LWC than in the reference case ($\hat{r}_l$ (max) $= 0.26$ g m^{-3} versus $\hat{r}_l$ (max) $= 0.32$ g m^{-3}). The increase of E occurs after 60 min, as opposed to 90 min in the reference case. That means that surface heat flux changes sign earlier and that in the subsidence case the CTBL cools faster. However, at first sight one would expect the subsidence case to cool less rapidly than the reference case due to the advection of warm
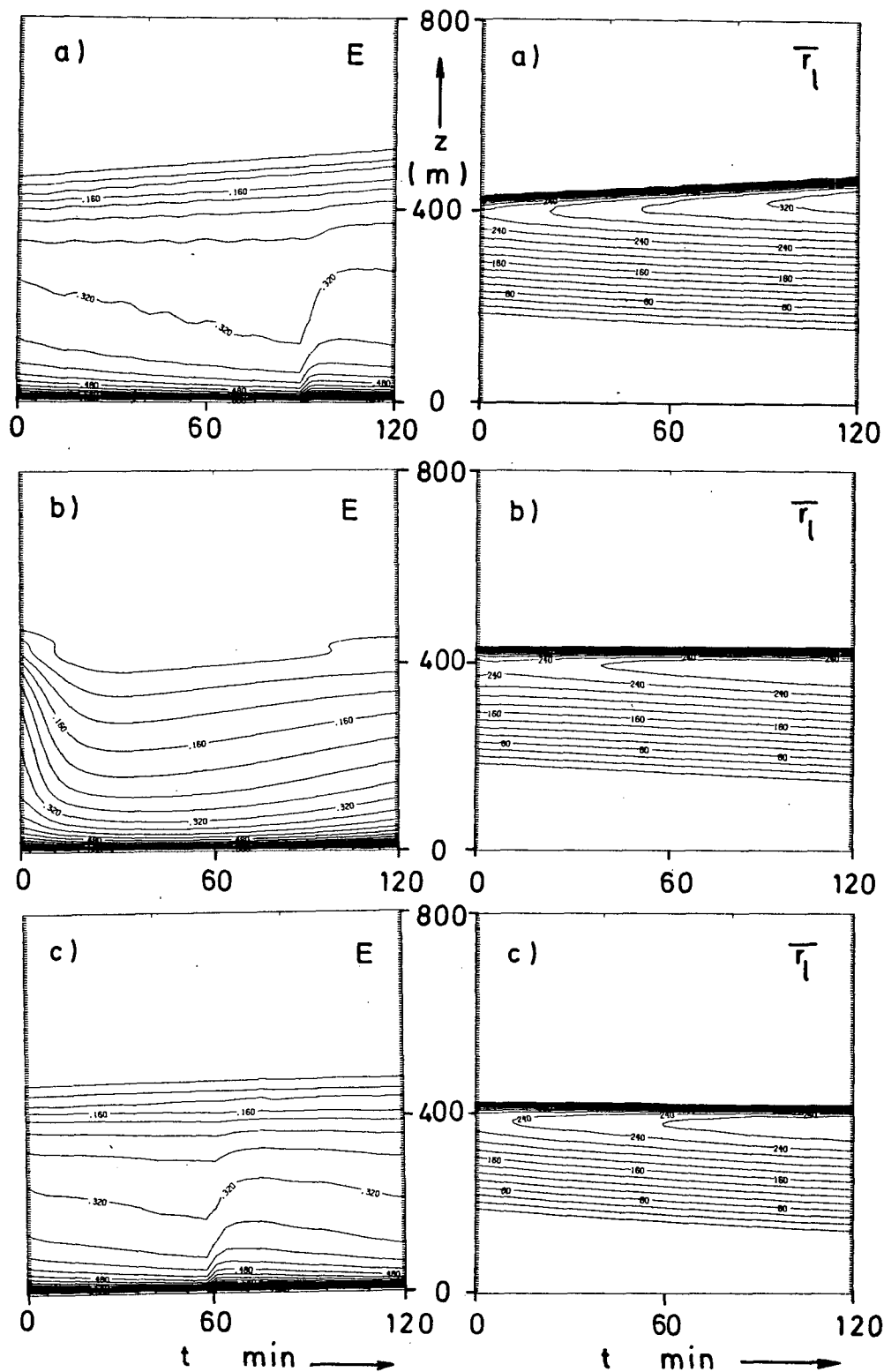
FIG. 16. Time-dependent vertical evolution of turbulence intensity and of liquid water content. In the left hand panel contour lines are given for E in $m^2 s^{-2}$, the contour intervals are 0.04 $m^2 s^{-2}$. In the right hand panel contour lines are given for $\bar{r}_l$ in 10^3 g m^{-3}, the contour intervals are 20×10^3 g m^{-3}. Three cases are considered: (a) reference case, (b) case with neglected radiation and (c) case with radiation and large scale subsidence considered.

TABLE 2. Turbulence kinetic energy with and without radiation; considered radiation E_{cr}, nonradiation case E_{nr} in $m^2 s^{-2}$ after 1 h of simulation; $\Delta E = ((E_{cr} - E_{nr})/E_{cr})$ in percent.

z/z_i	E_{cr}	E_{nr}	ΔE
1.0	0.14	0.01	93
0.9	0.22	0.03	86
0.8	0.24	0.06	75
0.7	0.29	0.09	69
0.6	0.30	0.13	43
0.5	0.31	0.18	42
0.4	0.31	0.19	39
0.2	0.35	0.27	23

air from the free atmosphere. What are the reasons for this surprising result? A more detailed analysis of the balance of the temperature θ_l shows that the mean subsidence warms mainly the inversion layer due to the strong gradient of the potential liquid temperature. Radiative cooling near cloud top is partly compensated by this heating and as a consequence the turbulent entrainment of warm air from the free atmosphere above is reduced. This is revealed by the weaker minimum of $\rho c_p \overline{w'\theta'_l}|_{z_i}$ and by a shift of its maximum to a lower height (Fig. 17b). The reduction of turbulent heating near the inversion is stronger than the warming due to the mean subsidence. As a net effect, the CTBL with subsidence cools faster than the reference case. Moreover, the turbulent humidity flux (Fig. 17c) is nearly constant with height, i.e. the turbulent humidity export at cloud top now balances the import at the surface. But due to the mean downward advection of dry air, the total water content is less than that of the reference case. As a consequence the cloud layer deepens slowly toward the surface and has a lower liquid water concentration than the reference case.

Chen and Cotton (1987) performed similar numerical experiments on stratus cloud development as function of radiative processes and subsidence. Gen-

erally, our results are in agreement with their results, especially the non-radiation case with the overall negative turbulent heat flux and reduced liquid water content. On the other hand, their cases with subsidence have liquid water contents that range between those of their reference and no radiation case. The deviation of our results in the subsidence case is probably caused by the different vertical structure of temperature, humidity and vertical velocity used in both calculations.

6. Conclusions

The vertical structure of turbulence within the quasistationary CTBL has been analyzed by use of observational data as well as numerical calculations. High frequency measurements of atmospheric state parameters, cloud physical parameters, and radiative fluxes have been carried out with the meteorological research aircraft 'Falcon' during MIZEX 1984 (Marginal Ice Zone Experiment) over the Greenland Sea. The measurements represent the first data set for the European part of the Arctic that gives a detailed insight into the turbulent mixing process. Moreover, a one dimensional statistical turbulence model with second-order closure has been developed. The measured profiles of the first, second and third moments of momentum, humidity and temperature are compared to our model calculations in order to verify basic model assumptions.

Our main results from the analysis of the observations during the Arctic stratus event from 26 June 1984 are:

• The horizontal wind speed is within the range of about 10 m s^{-1}. The wind shear near the surface and cloud top promotes turbulent mixing that cannot be neglected.

• The measurements reveal a well developed horizontal homogeneity of turbulence structure within Arctic stratus clouds. This is shown by the agreement of second-order moments which are calculated for dif-
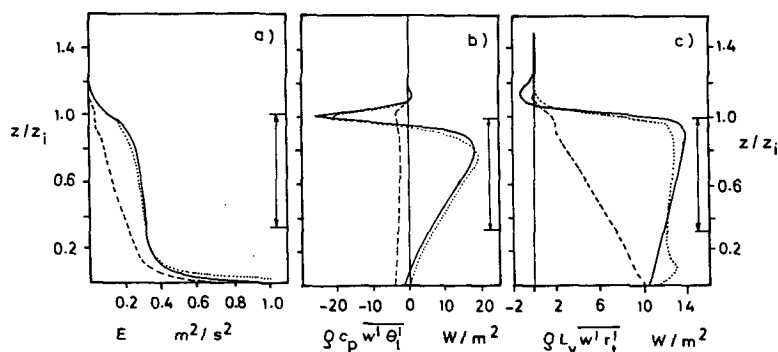

FIG. 17. Profiles of turbulence kinetic energy, sensible and latent heat fluxes under different constraints after one hour of simulation time. The reference case is marked by the solid line, the nonradiation case by the dashed line and the subsidence case is marked by the dotted line.
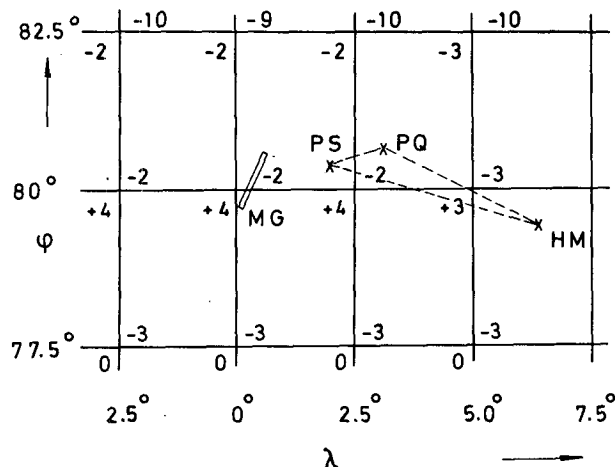
FIG. 18. Geographical grid with a size of 2.5° × 2.5° covering the area of the measurements of 26 June 1984. λ, φ denote geographical longitude and latitude, MG the area of aircraft measurements while PS, PQ, HM denote the positions of the research vessels 'Polarstern', 'Polarqueen', 'Hakon Mosby' respectively. The results of the ECMWF analysis for the vertical velocity are given at every grid point in mm s^{-1}: numbers in the upper right refer to 850 hPa and in the lower left to 1000 hPa.

ferent parts of each horizontal flight leg. Also, the nearly constant cloud drop concentration along such flight legs confirms this fact.

From the budgets of temperature and second-order moments calculated from measurements and numerical simulations we obtain the following results:

• The comparison of measurements and calculations shows good agreement for the vertical profiles of the mean variables, vertical velocity variance, variances of thermodynamic variables and turbulent fluxes of heat and humidity.

• The largest deviations arise for the variance of the horizontal wind components near and below the inversion. This is caused by the incorrect formulation of the length scale. However, in spite of these deviations our model represents a useful tool for the investigation of the quasi-stationary Arctic CTBL.

• Near the surface the turbulent fluxes of heat and humidity are of only minor importance once Arctic stratus clouds have developed. On the other hand, the profiles of the mean wind speed and the fluxes of momentum lead to a high level of turbulence kinetic energy.

• The cloud top has been identified as the region that controls the entire cloud layer. For fully developed Arctic stratus clouds the positive heat flux within the cloud is caused by radiative cooling that attains maximum values in the upper 20 m of the cloud. The energy that is necessary to maintain entrainment against the thermal stability is delivered from the shear-produced horizontal velocity variance. Part of this hori-

zontal variance is transferred to the vertical velocity variance via the pressure velocity correlation.

• At the inversion height the vertical turbulent transport of second-order moments and the transport by pressure velocity correlations are of the same order of magnitude as those due to shear and buoyancy effects. The diffusive processes that have been investigated export the corresponding second-order moments from the CTBL into the free atmosphere.

• The closure assumption used for integrating the mixed layer model of Kraus and Schaller (1978a) has been tested. It is shown the entrainment process is underestimated in their model and therefore the vertical development of the cloud layer is overestimated.

Based on the simulations alone the following conclusions can be drawn:

• When radiative processes are not considered the original turbulence structure breaks down and a new balance is established. Near the cloud top the turbulence energy is reduced by about 90%, and near the surface by about 23%. The turbulent fluxes decrease to very low values. Wind shear alone is not able to maintain an efficient turbulent exchange in this case.

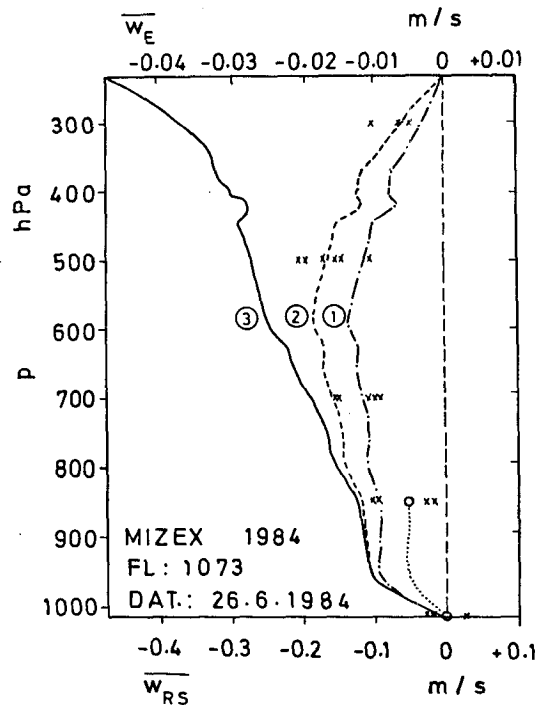• Large-scale subsidence can prevent the cloud top

FIG. 19. Profiles of mean vertical velocity calculated from radio soundings (lines, lower scale) and ECMWF analysis (crosses, upper scale). Lines marked by 1 and 2 present the results by the correction after O'Brien (1970), line 3 is the unadjusted result. The number of crosses of ECMWF data differs from level to level because some datapoints are identical. The circles correspond to the averages of the crosses for one level, while the dotted line denotes the mean estimated profile of the vertical velocity for the lower troposphere.

from rising, but the simultaneous change in the turbulence structure, especially of the heat flux, causes the total CTBL to cool faster than in the reference case (radiation included, no subsidence).

The results presented in this paper refer to only one case of well developed AS clouds. Nevertheless, we consider this case as an instructive example in order to clearly identify different interacting physical processes.

There are still questions related to the formation and dissipation of ASC that might be answered with the aid of calculations with our model. A parameter study should allow the determination of the effect of high level clouds on the structure of the Arctic CTBL. From a modeling point of view, the question is still open as to how to appropriately formulate the turbulent length scale. A solution to this problem might arise from large eddy simulations. For the case of the dry CBL, Schmidt and Schumann (1988) showed that there are two different length scales, one for the well mixed and one for the inversion layer. Corresponding calculations should be carried out also for the CTBL. We could not determine the possible influence of breaking waves on the entrainment process itself. For this purpose measurements under special conditions were made during a recent experiment in the Arctic region in May 1988 (ARKTIS 88). The analysis of these data is now in progress. Large eddy simulations should also be performed, as was done by Carruthers and Moeng (1987). Another remaining question concerns the dissipation of ASC. This process may be caused by the interaction of both synoptic and microscale effects, but this needs further investigation.

APPENDIX

1. Realizability of second-order moments in numerical simulation

The used model parameterizations can lead to nonphysical solutions for the turbulent flow. In order to prevent such an effect, André et al. (1976) and Schumann (1977) introduced the following realizability conditions:

1) $\overline{a'^2} \geqslant 0.0$; to suppress oscillations of the solution around zero, the criteria is strengthened to: $\overline{a'^2} \geqslant 10^{-3} \cdot \overline{a'^2}|_{max}$

2) $|\overline{a'b'}| \leqslant \sqrt{\overline{a'^2} \cdot \overline{b'^2}}$

3) $\det(R_{ij}) \geqslant 0.0$,

where a' and b' stand for u_i', θ_l' and r_t', $\overline{a'^2}|_{max}$ is the maximum value of each profile, and R_{ij} is the Reynolds stress tensor.

2. List of symbols

ASC	Arctic stratus cloud
CTBL	Cloud-topped boundary layer
ECMWF	European Center for Medium-range Weather Forecast
MIZEX 84	Marginal Ice Zone Experiment 1984
PBL	Planetary boundary layer
SOC	Second-order closure
TKE	Turbulent kinetic energy
UTC	Universal Time Coordinated
a, b	any variable
c_p	specific heat of dry air at constant pressure
E	turbulent kinetic energy, $E = 0.5(\overline{u'^2} + \overline{v'^2} + \overline{w'^2})$
f	Coriolis parameter, frequency
g	constant of gravitation
l	turbulence length scale
l_u, l_d	turbulence length scale upwards and downwards
L	Obuchov length, $L = -u_*^3 \theta / (g\kappa\overline{w'\theta'})$
L_v	latent heat of water vapour
p	pressure
q^2	twice the turbulence kinetic energy $q^2 = (\overline{u'^2} + \overline{v'^2} + \overline{w'^2}) = 2E$
$\overline{r}, \overline{r_l}, \overline{r_t}, \overline{r_{sat}}$	mean mixing ratios of water vapor, liquid water, total water and mixing ratio at saturation point
$\hat{r}_l, \hat{r}_{ad}$	mean liquid water content $\hat{r}_l = \rho \cdot \overline{r_l}$, adiabatic liquid water content
r_*	scaling factor of humidity, $r_* = -\overline{w'r'}/u_*$
R	net radiation flux
R_{ij}	Reynolds-stress tensor
R_a, R_v	specific gas constants for air and water vapor
$R_E, R_w, R_{w\theta}, R_\theta$	residuals of balance equations
S_u	spectral density of variance $\overline{u'^2}$
T_0, T, T_s	reference temperature, temperature, surface temperature
x, y, z, x_i	Cartesian coordinates, $i = 1, 2, 3$
$\overline{u}, \overline{v}, \overline{w}, \overline{u_i}$	mean components of the velocity vector $i = 1, 2, 3$
u_F	mean aircraft speed of the 'Falcon' $u_F \approx 100$ m s^{-1}

$\overline{u_g}, \overline{v_g}$	components of geostrophic wind
u_*	friction velocity, $u_* = ((\overline{u'w'})^2 + \overline{(v'w')}^2)^{1/4}$
$\overline{w_E}, \overline{w_{RS}}$	mean vertical velocity derived from data of ECMWF and of radiosonde soundings
z_b, z_i	height of cloud base, height of boundary layer
z_0	roughness length
β_1	buoyancy coefficient for temperature $\beta_1 = 1/T_0$
β_2	buoyancy coefficient for water vapor $\beta_2 = (R_v/R_a - 1)$
β_3	buoyancy coefficient for liquid water content $\beta_3 = ((L_v/c_p T) - (R_v/R_a))$
Δh_i	thickness of the layer of temperature inversion
$\Delta z, \Delta t$	grid size, time step
ϵ	dissipation rate of turbulence kinetic energy
$\epsilon_u, \epsilon_v, \epsilon_w$	dissipation rates of variances of momentum
κ	von Kármán constant, $\kappa = 0.35$
ρ	density
$\theta, \theta_l, \theta_v$	potential temperature, liquid water potential temperature, virtual potential temperature
θ_*	scaling factor for temperature, $\theta_* = -\overline{w'\theta'}/u_*$

REFERENCES

André, J. C., G. De Moor, P. Lacarrère, G. Therry and G. Du Vachat, 1976: Turbulence approximation for inhomogeneous flows: Part I: The clipping approximation. *J. Atmos. Sci.*, **33**, 476–481.

Best, A. C., 1951: Drop size distributions in clouds and fog. *Quart. J. Roy. Meteor. Soc.*, **77**, 418–426.

Betts, A. K., 1973: Non-precipitating cumulus convection and its parameterization. *Quart. J. Roy. Meteor. Soc.*, **99**, 178–196.

Bougeault, P., 1985: The diurnal cycle of the marine stratocumulus layer: A higher-order model study. *J. Atmos. Sci.*, **42**, 2826–2843.

Brost, R. A., J. C. Wyngaard and D. H. Lenschow, 1982: Marine stratocumulus layers. Part II: Turbulence budgets. *J. Atmos. Sci.*, **39**, 818–836.

Busch, N., U. Ebel, H. Kraus and E. Schaller, 1982: The structure of the subpolar inversion-capped ABL. *Arch. Met. Geophys. Bioklim.*, Ser. A, **31**, 1–18.

Carruthers, D. J., and C. H. Moeng, 1987: Waves in the overlaying inversion of the convective boundary layer. *J. Atmos. Sci.*, **44**, 1801–1808.

Chen, C., 1985: The physics of the marine stratocumulus-capped mixed layer. Dissertation, Res. Institute of Colorado.

——, and W. R. Cotton, 1983a: A one-dimensional simulation of the stratocumulus-capped mixed layer. *Bound.-Layer. Meteor.*, **25**, 289–321.

——, and ——, 1983b: Numerical experiments with a one-dimensional higher order turbulence model: Simulation of the Wangara Day 33, *Bound.-Layer. Meteor.*, **25**, 375–404.

——, and ——, 1987: The physics of the marine stratocumulus-capped mixed layer. *J. Atmos. Sci.*, **44**, 2951–2977.

Curry, J. A., 1986: Interactions among turbulence, radiation and

microphysics in Arctic stratus clouds. *J. Atmos. Sci.*, **43**, 90–106.

——, and G. F. Herman, 1985: Relationships between large–scale heat and moisture budgets and the occurrence of Arctic stratus clouds. *Mon. Wea. Rev.*, **113**, 1441–1457.

——, E. E. Ebert and G. F. Herman, 1988: Mean and turbulence structure of the summertime Arctic cloudy boundary layer. *Quart. J. Roy. Meteor. Soc.*, **114**, 715–746.

Deardorff, J. W., 1976: Usefulness of liquid-water potential temperature in a shallow-cloud model. *J. Appl. Meteor.*, **15**, 98–102.

——, and G. E. Willis, 1985: Further results from a laboratory model of the convective planetary boundary layer. *Bound.-Layer. Meteor.*, **32**, 205–236.

Dergach, A. I., G. M. Zabrodsky and V. G. Morachevsky, 1960: The results of a complex investigation of the type St-Sc cloud and fogs in the Arctic. *Bull. Acad. Sci. USSR Geophys. Ser.*, **1**, 66–70.

Dolgin, I. M., 1960: Arctic aero-climatological studies. *Probl. Arktiki. Antarkt.*, **4**, 64–75.

Duynkerke, P. G., and A. G. M. Driedonks, 1987: A model for the turbulent structure of the stratocumulus-topped atmospheric boundary layer. *J. Atmos. Sci.*, **44**, 43–64.

Finger, J. E., and H. Schmidt, 1986: On the efficiency of higher order turbulence models simulating the convective boundary layer. *Beitr. Phys. Atmos.*, **59**, 505–517.

Forkel, R., and P. Wendling, 1986: A numerical study of the formation of Arctic stratus clouds with consideration of absorbing aerosol particles. *Meteor. Rundsch.*, **59**, 74–79.

Guest, P. S., and K. L. Davidson, 1987: The effect of observed ice conditions on the drag coefficient in the summer east Greenland Sea marginal ice zone. *J. Geophys. Res.*, **92**, 6943–6954.

Hänel, G., and M. Lehmann, 1981: Equilibrium size of aerosol particles and relative humidity: New experimental data from various aerosol types and their treatment for cloud physics application. *Beitr. Phys. Atmos.*, **54**, 57–70.

Hauf, T., 1984: Turbulenzmessungen mit dem Forschungsflugzeug 'Falcon.' *Meteor. Rundsch.*, **37**, 163–176.

Herman, G., 1977: Solar radiation in summertime Arctic stratus clouds. *J. Atmos. Sci.*, **34**, 1423–1432.

——, 1980: Thermal radiation in Arctic stratus clouds. *Quart. J. Roy. Meteor. Soc.*, **106**, 771–780.

——, and R. Goody, 1976: Formation and persistence of summertime Arctic stratus clouds. *J. Atmos. Sci.*, **33**, 1537–1553.

——, and J. A. Curry, 1984: Observational and theoretical studies of solar radiation in Arctic stratus clouds. *J. Climate Appl. Meteor.*, **23**, 5–24.

Huschke, R. E., 1969: Arctic cloud statistic from 'air-calibrated' surface weather observations. RAND Memo. RM-6273-PR, 79 pp.

Johannessen, O. M., 1987: Introduction: Summer marginal ice zone experiment during 1983 and 1984 in the Fram Strait and the Greenland Sea. *J. Geophys. Res.*, **92**, 6716–6718.

Kraus, H., and E. Schaller, 1978a: Steady-state characteristics of inversions capping a well-mixed planetary boundary layer. *Bound.-Layer. Meteor.*, **14**, 83–104.

——, and ——, 1978b: A note on the closure in Lilly-type inversion models. *Tellus*, **30**, 284–288.

Launder, B. E., G. J. Reece and W. Rodi, 1975: Progress in the development of a Reynolds stress turbulence closure. *J. Fluid Mech.*, **80**, 537–566.

Lilly, D. K., 1968: Models of cloud-topped mixed layers under a strong inversion. *Quart. J. Roy. Meteor. Soc.*, **94**, 292–309.

McDonald, J., 1963: The saturation adjustment in numerical modelling of fog. *J. Atmos. Sci.*, **20**, 476–478.

Meischner, P., 1985: User's manual for the 'Falcon' system. ESA-TT-936. [Obtainable from European Space Research Institute, 00044 Frascati, Italy].

Mellor, G. L., and T. Yamada, 1974: A hierarchy of turbulence closure models for planetary boundary layers. *J. Atmos. Sci.*, **31**, 1791–1806.

Moeng, C. H., 1986: Large-eddy simulation of a stratus-topped

boundary layer. Part I: Structure and budgets, *J. Atmos. Sci.,* **43,** 2886–2900.

——, and A. Arakawa, 1980: A numerical study of a marine subtropical stratus cloud layer and its stability. *J. Atmos. Sci.,* **37,** 2661–2676.

——, and D. A. Randall, 1984: Problems in simulating the stratocumulus-topped boundary layer with a third-order closure model. *J. Atmos. Sci.,* **41,** 1588–1600.

Nicholls, S., 1984: The dynamics of stratocumulus: Aircraft observations and comparison with a mixed layer model. *Quart. J. Roy. Meteor. Soc.,* **110,** 783–820.

O'Brien, J. J., 1970: Alternative solutions to the classical vertical velocity problem. *J. Appl. Meteor.,* **9,** 197–203.

Oliver, D. A., W. S. Lewellen and G. G. Williamson, 1978: The interaction between turbulent and radiative transport in the development of fog and low-level stratus. *J. Atmos. Sci.,* **35,** 301–316.

Otha, S., 1982: A numerical case study of Arctic stratus in July 1975. *Nat. Inst. Polar. Res., Mem., Spec. Issue,* (Jpn), 133–143.

Randall, D. A., 1984: Buoyant production and consumption of turbulence kinetic energy in cloud-topped mixed layers. *J. Atmos. Sci.,* **41,** 402–413.

Rotta, J., 1951: Statistische Theorie nichthomogener Turbulenz. *Z. Phys.,* **129,** 547–572.

Schmidt, H., and U. Schumann, 1989: Coherent structure of the convective boundary layer derived from large-eddy simulations. *J. Fluid Mech.,* **200,** 511–562.

Schubert, W. H., J. S. Wakefield, E. J. Steiner and S. K. Cox, 1979: Marine stratocumulus convection. Parts I and II, *J. Atmos. Sci.,* **36,** 1286–1324.

Schumann, U., 1977: Realizability of Reynolds-stress turbulence models. *Phys. Fluids,* **20,** 721–725.

Shine, K. P., and R. G. Crane, 1984: The sensitivity of a one-dimensional thermodynamic sea ice model to changes in cloudiness. *J. Geophys. Res.,* **89,** 10615–10622.

Tsay, S. C., and K. Jayaweera, 1984: Physical characteristics of Arctic stratus clouds. *J. Climate Appl. Meteor.,* **23,** 584–596.

Wyngaard, J. C., 1973: *Workshop on Micrometeorology.* Amer. Meteor. Soc., 47 pp.

Zdunkowski, W., W. Panhans, R. Welch and G. Korb, 1982: A radiational scheme for circulation and climate models. *Beitr. Phys. Atmos.,* **55,** 215–237.

Zeman, O., and J. L. Lumley, 1976: Modeling buoyancy driven mixed layers. *J. Atmos. Sci.,* **33,** 1974–1988.